

AD-786 450

FEASIBILITY STUDY OF EXOELECTRON
IMAGING AS AN NDT METHOD FOR LASER
SURFACE DAMAGE OF NONLINEAR OPTICAL
MATERIALS AND LASER GLASS

Peter F. Braunlich

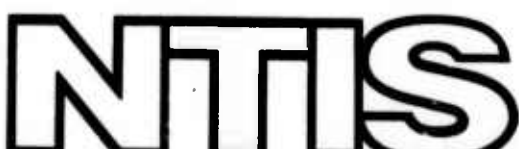
Bendix Research Laboratories

Prepared for:

Air Force Cambridge Research Laboratories
Defense Advanced Research Projects Agency

August 1974

DISTRIBUTED BY:



National Technical Information Service
U. S. DEPARTMENT OF COMMERCE
5285 Port Royal Road, Springfield Va. 22151

UNCLASSIFIED
Security Classification

AD 786 450

DOCUMENT CONTROL DATA - R&D

(Security classification of title, body of abstract and indexing annotation must be entered when the overall report is classified)

1 ORIGINATING ACTIVITY (Corporate author)	2a REPORT SECURITY CLASSIFICATION
Bendix Research Laboratories Bendix Center Southfield, Michigan 48076	Unclassified
2b GROUP	

3 REPORT TITLE

FEASIBILITY STUDY OF EXOELECTRON IMAGING AS AN NDT METHOD FOR LASER SURFACE DAMAGE OF NONLINEAR OPTICAL MATERIALS AND LASER GLASS

4 DESCRIPTIVE NOTES (Type of report and inclusive dates)

Scientific. Final. For the period 8-15-72 through 2-14-74

Approved

11 July 1974

5 AUTHOR(S) (Last name, first name, initial)

Peter F. Braunlich

6 REPORT DATE

August 1974

7a TOTAL NO OF PAGES

80

7b NO OF REFS

47

8a CONTRACT OR GRANT NO. ARPA Order No. 2042
F19628-73-C-0032

9a ORIGINATOR'S REPORT NUMBER(S)

b PROJECT NO Task, Work Unit Nos.
2042 n/a n/a
c DOD Element 62701E
d DOD Subelement n/a

7133

9b OTHER REPORT NO(S) (Any other numbers that may be assigned
this report)

AFCRL-TR-74-0266

10 AVAILABILITY/LIMITATION NOTICES

A - Approved for public release; distribution unlimited.

11 SUPPLEMENTARY NOTES

This research was sponsored by the
Defense Advanced Research Projects
Agency.

12 SPONSORING MILITARY ACTIVITY

Air Force Cambridge Research
Laboratories (LQ)
Hanscom AFB, Massachusetts 01730

13 ABSTRACT

This report presents the results of an eighteen-month study of exoelectron emission from dielectric materials used in high power laser systems.

The work was performed to gain information on general exoelectron properties of optical materials particularly after exposure to intense laser pulses below and just above the damage threshold and to assess the feasibility of exoelectron techniques as NDT methods for laser surface damage.

A phenomenological theory of the electron kinetic processes leading to electron trapping, exoelectron emission, and, ultimately, at very high photon fluxes, to intrinsic damage, was developed.

This theory provided further insight in the intrinsic damage mechanism. Avalanche ionization was confirmed to be the dominant mechanism of intrinsic laser breakdown in NaCl. The roles of lattice defects (Cl⁻-vacancies), F-centers and of multiphoton photocarrier generation was investigated. They were found to lower the intrinsic damage threshold. Detailed calculations of the pulse length dependence of the damage threshold, the time of occurrence of breakdown during the laser pulse, and the laser-induced spatial trap distribution were performed.

Reproduced by
NATIONAL TECHNICAL
INFORMATION SERVICE
U S Department of Commerce
Springfield VA 22151

DD FORM 1 JAN 64 1473

UNCLASSIFIED
Security Classification

UNCLASSIFIED
Security Classification

16. KEY WORDS	LINK A		LINK B		LINK C	
	ROLE	WT	ROLE	WT	ROLE	WT
Pyroelectric materials Laser surface damage threshold LiNbO_3 Thermally stimulated field emission Exoelectron emission Laser optical materials Dielectric materials						
INSTRUCTIONS						
<p>1. ORIGINATING ACTIVITY: Enter the name and address of the contractor, subcontractor, grantees, Department of Defense activity or other organization (corporate author) issuing the report.</p> <p>2a. REPORT SECURITY CLASSIFICATION: Enter the overall security classification of the report. Indicate whether "Restricted Data" is included. Marking is to be in accordance with appropriate security regulations.</p> <p>2b. GROUP: Automatic downgrading is specified in DoD Directive 5200.10 and Armed Forces Industrial Manual. Enter the group number. Also, when applicable, show that optional markings have been used for Group 3 and Group 4 as authorized.</p> <p>3. REPORT TITLE: Enter the complete report title in all capital letters. Titles in all cases should be unclassified. If a meaningful title cannot be selected without classification, show title classification in all capital letters in parenthesis immediately following the title.</p> <p>4. DESCRIPTIVE NOTES: If appropriate, enter the type of report, e.g., interim, progress, summary, annual, or final. Give the inclusive dates when a specific reporting period is covered.</p> <p>5. AUTHOR(S): Enter the name(s) of author(s) as shown on or in the report. Enter last name, first name, middle initial. If military, show rank and branch of service. The name of the principal author is an absolute minimum requirement.</p> <p>6. REPORT DATE: Enter the date of the report as day, month, year, or month, year. If more than one date appears on the report, use date of publication.</p> <p>7a. TOTAL NUMBER OF PAGES: The total page count should follow normal pagination procedures, i.e., enter the number of pages containing information.</p> <p>7b. NUMBER OF REFERENCES: Enter the total number of references cited in the report.</p> <p>8a. CONTRACT OR GRANT NUMBER: If appropriate, enter the applicable number of the contract or grant under which the report was written.</p> <p>8b, 8c, & 8d. PROJECT NUMBER: Enter the appropriate military department identification, such as project number, subproject number, system numbers, task number, etc.</p> <p>9a. ORIGINATOR'S REPORT NUMBER(S): Enter the official report number by which the document will be identified and controlled by the originating activity. This number must be unique to this report.</p> <p>9b. OTHER REPORT NUMBER(S): If the report has been assigned any other report numbers (either by the originator or by the sponsor), also enter this number(s).</p>						
<p>10. AVAILABILITY/LIMITATION NOTICES: Enter any limitations on further dissemination of the report, other than those imposed by security classification, using standard statements such as:</p> <p>(1) "Qualified requesters may obtain copies of this report from DDC."</p> <p>(2) "Foreign announcement and dissemination of this report by DDC is not authorized."</p> <p>(3) "U. S. Government agencies may obtain copies of this report directly from DDC. Other qualified DDC users shall request through _____."</p> <p>(4) "U. S. military agencies may obtain copies of this report directly from DDC. Other qualified users shall request through _____."</p> <p>(5) "All distribution of this report is controlled. Qualified DDC users shall request through _____."</p> <p>If the report has been furnished to the Office of Technical Services, Department of Commerce, for sale to the public, indicate this fact and enter the price, if known.</p> <p>11. SUPPLEMENTARY NOTES: Use for additional explanatory notes.</p> <p>12. SPONSORING MILITARY ACTIVITY: Enter the name of the departmental project office or laboratory sponsoring (paying for) the research and development. Include address.</p> <p>13. ABSTRACT: Enter an abstract giving a brief and factual summary of the document indicative of the report, even though it may also appear elsewhere in the body of the technical report. If additional space is required, a continuation sheet shall be attached.</p> <p>It is highly desirable that the abstract of classified reports be unclassified. Each paragraph of the abstract shall end with an indication of the military security classification of the information in the paragraph, represented as (7S), (S), (C), or (U).</p> <p>There is no limitation on the length of the abstract. However, the suggested length is from 150 to 225 words.</p> <p>14. KEY WORDS: Key words are technically meaningful terms or short phrases that characterize a report and may be used as index entries for cataloging the report. Key words must be selected so that no security classification is required. Identifiers, such as equipment model designation, trade name, military project code name, geographic location, may be used as key words but will be followed by an indication of technical context. The assignment of links, rules, and weights is optional.</p>						

ARPA Order No. 2042

Program Code No. 2D1

Contractor: Bendix Research Laboratories

Effective Date of Contract: 15 August 1972

Contract No. F19628-73-C-0032

Principal investigator and Phone Number: Dr. Peter F. Braunlich
(313) 352-7725

AFCRL Project Scientist and Phone Number: John V. Nikula
(617) 861-3532

Contract Expiration Date: 14 February 1974

ACCESSION FORM	
PTIS	WHITE SECTION
ORC	E. K. Schmitz
UNARMED	<input checked="" type="checkbox"/>
JUSTIFICATION	<input type="checkbox"/>
BY.....	
DISTRIBUTION/AVAILABILITY CODES	
DIST.	AVAIL. AND/OR SPECIAL
A	

Qualified requestors may obtain additional copies from the Defense Documentation Center. All others should apply to the National Technical Information Service.

1b

ABSTRACT

We have investigated exoelectron emission from Nd-2 laser glass, lithium niobate, lithium fluoride, and sodium chloride in high vacuum after excitation with several-keV electrons, with uv, and with pulses from Q-switched Nd- and ruby-lasers. Exoelectron emission was measured either with channel electron multipliers and single-pulse counting techniques, or with the aid of channel plate multiplier bundles having high gain and spatial resolution.

The work was performed to gain information on general exoelectron properties of optical materials particularly after exposure to intense laser pulses below and just above the damage threshold and to assess the feasibility of exoelectron techniques as NDT methods for laser surface damage. We observed emission of negatively charged particles from all investigated materials after electron bombardment. LiNbO_3 exhibits a newly discovered effect subsequently termed "thermally stimulated field emission of electrons." This strong emission which occurs without previous exposure of the sample to any ionizing radiation prevented the observation of laser-induced thermally stimulated exoelectron emission. In general, laser-induced exoelectron emission was either not observed at all (as in Nd-2 glass and LiNbO_3), found to be caused by unexpected plasma effects (as in LiF), or was too weak to be of any use as a NDT-technique.

A phenomenological theory of the electron kinetic processes leading to electron trapping, exoelectron emission, and, ultimately, at very high photon fluxes, to intrinsic damage, was developed.

This theory provided further insight in the intrinsic damage mechanism. Avalanche ionization was confirmed to be the dominant mechanism of intrinsic laser breakdown in NaCl. The roles of lattice defects (Cl^- -vacancies), F-centers and of multiphoton photocarrier generation was investigated. All three were found to lower the intrinsic damage threshold. Detailed calculations of the pulse length dependence of the damage threshold, the time of occurrence of breakdown during the laser pulse, and the laser-induced spatial trap distribution were performed.

TABLE OF CONTENTS

	<u>Page</u>
SECTION 1 - INTRODUCTION	1
SECTION 2 - EXOELECTRON EMISSION FROM DIELECTRIC MATERIALS	5
2.1 General Remarks	5
2.2 Exoelectron Mechanism	8
SECTION 3 - LASER INDUCED DAMAGE IN SOLIDS	11
3.1 The Damage Mechanism	11
3.2 Correlations Between Laser Surface Damage and Exoelectron Emission	11
SECTION 4 - ELECTRON KINETICS OF INTRINSIC LASER DAMAGE AND EXOELECTRON EMISSION	15
4.1 General Formalism	15
4.2 Application to Intrinsic Damage Induced by Ruby Laser Radiation in Sodium Chloride	19
4.2.1 Rate Equations	19
4.2.2 Photon Induced Transition Rates	23
4.2.3 The Avalanche Ionization Rate	24
4.2.4 Thermal Transition Rates	25
4.2.5 Numerical Calculations - General Remarks	26
4.2.6 Generation of Free Carriers and Damage Mechanism in NaCl	27
4.2.7 Recombination of Free Carriers After Exposure of NaCl to Laser Pulse	40
4.2.8 Diffusion Effects	47
4.2.9 Laser Induced Exoelectron Emission	49
4.3 Application to NDT of Laser Surface Damage	49
SECTION 5 - EXPERIMENTAL FACILITIES FOR MEASUREMENT OF GENERAL EXOELECTRON EMISSION PROPERTIES OF LASER MATERIALS	51
5.1 Exoelectron Emission Test Facilities	52
5.2 Experiments With LiF	57
5.3 Summary of EE-Experiments on Laser Glasses, Sodium Chloride, and Lithium Niobate	64
SECTION 6 - CONCLUDING REMARKS	71
SECTION 7 - ACKNOWLEDGEMENTS	73
SECTION 8 - REFERENCES	75

LIST OF ILLUSTRATIONS

<u>Figure No.</u>	<u>Title</u>	<u>Page</u>
1	Schematic energy level diagram of NaCl.	20
2	Normalized concentration n_c/N_t of free electrons in NaCl containing 5×10^{16} Cl ⁻ -vacancies as a function of laser peak flux A^* for 60 nsec ruby laser pulses.	28
3	Normalized concentration n_c/N_t of free electrons in NaCl containing 5×10^{16} cm ⁻³ Cl ⁻ -vacancies as a function of laser peak flux A^* for ruby laser pulses of several different pulse lengths t_p .	32
4	Pulse length dependence of the peak ruby laser flux required to induce intrinsic damage in NaCl at the end of the laser pulse.	35
5	Dependence of the intrinsic damage threshold on the ruby laser pulse duration for NaCl; damage criterion: $n_c = 1 \times 10^{18}$ cm ⁻³ .	37
6	The rise of the free electron concentration and of the temperature during the exposure of a NaCl crystal with a uniform 60 nsec pulse from a ruby laser having a peak flux of $A^* = 1.865 \times 10^{28}$ photons per cm ² and sec.	39
7	Time of intrinsic damage occurrence as a function of the peak flux.	41
8	Laser induced concentration of F-center in a NaCl crystal containing 5×10^{16} Cl ⁻ -vacancies as a function of the ruby laser peak flux for various initial F-center densities.	43
9	Spatial distribution of F-centers along the surface of a NaCl crystal that was exposed to a 60 nsec ruby laser pulse having a peak flux of $A^* = 2 \times 10^{28}$ photons per cm ² and sec.	45
10	Laser flux profile and normalized temperature profile of the standard NaCl crystal that was exposed at room temperature to a 60 nsec TEM ₀₀ mode ruby laser pulse having a peak flux $A^* = 2 \times 10^{28}$ photons per cm ² and sec.	46
11	Schematic diagram of the general exoelectron emission test system.	53
12	Exoelectron imaging system.	55
13	Schematic diagram of the laser-induced exoelectron emission and surface damage facility.	56
14	Schematic diagram of apparatus used in studied of OSEE from laser-irradiated samples.	58

<u>Figure No.</u>	<u>Title</u>	<u>Page</u>
15	Surface damage (a) and corresponding TSEE images (b) obtained from LiF after exposure to Q-switched 30-nsec pulses (multi-mode) from a Nd-glass laser.	61
16	Exoelectron images of a LiF single crystal that was placed parallel to the axis of the laser beam waist so that the air breakdown spark occurred in front of the crystal as shown schematically.	63
17	TSEE from ED-2 glass after electron bombardment (3 keV, $6 \times 10^{-7} \text{ A/cm}^2$) for: (a) 10 min, (b) 150 sec, and (c) 0 sec.	65
18	TSEE for NaCl: (a) exoelectron emission after electron excitation, (b) emission emission with no prior electron excitation, and (c) temperature profile.	67
19	Negative charge emission from a fresh NaCl crystal without laser exposure.	68
20	Laser-induced exoelectron emission from a laser-grade NaCl crystal.	69

Table No.

I	The peak flux A^* of a 60 nsec ruby laser pulse required to produce a damaging concentration of $n_c = 10^{18} \text{ cm}^{-3}$ of free carriers in NaCl at the end of the pulse. Comparison of different mechanisms.	29
II	Definition of damage threshold.	34
III	Comparison of measured and calculated damage thresholds for NaCl at the ruby frequency.	38

SECTION 1

INTRODUCTION

Systematic studies of damage inflicted on optical materials by intense laser radiation has not only led to the development of materials with improved damage resistance but also to a fundamental understanding of the damage process itself.¹ Yet, little or no work was done to investigate the possibility of nondestructive testing of the susceptibility of a particular optical material to laser damage. Initial experiments on thermally stimulated emission of low energy electrons (exoelectrons) from a surface after exposure to laser radiation and apparent correlations between this emission and precursors of laser surface damage gave rise to hope, that exoelectron emission techniques might be developed to provide a tool for nondestructive testing of optical surfaces with respect to their laser damage threshold.²

In this report an 18-month program is described that was designed to investigate this aspect of laser induced exoelectron emission in more detail. The program consisted of two parts:

- Experimental investigation of general exoelectron emission properties of selected laser optical materials.
- Theoretical studies of the electron kinetic processes that occur in the solid during and after exposure to high power laser light.

The experimental work centered around unique exoelectron imaging techniques developed by Bendix.^{3,4} With the aid of exoelectron imaging it is possible to measure directly the density distribution of the emission current on the surface and to correlate it with the intensity profile of the laser pulse.

In the following sections we give a short review of exoelectron emission properties of dielectric materials, present a phenomenological theory of laser induced exoelectron emission and describe the facilities

that were assembled for the experiments performed on laser glass, lithium niobate, lithium fluoride, and sodium chloride.

In general, the execution of meaningful exoelectron experiments on optical surfaces was far more difficult than expected. Thermally or optically stimulated emission of charged particles was observed from the surfaces of nearly all investigated materials under a variety of conditions. Desorption of gas, changes of large parts of the surface after breakdown at only a small site, and light- and thermally-triggered physico-chemical reactions cause emissions that interfere with the observation of exoelectrons stemming from thermally or optically stimulated bleaching of color centers (traps). Recent work by Krylova^{5,6} confirms these findings. Exoelectron emission from, e.g., alkali-halides and metal oxides, is not caused exclusively by the release of electrons from traps in a thin layer, as generally agreed upon just a few years ago.^{7,8} Other processes may lead to charge emission as well. One of them is the formation of radicals in the adsorption layer during exposure to ionizing radiation (energetic photons or nuclear particles). Multiphoton ionization may produce similar effects in the case of intense laser radiation. Subsequent recombination of these radicals is believed to cause either spontaneous emission of charged particles or, upon thermal or optical stimulation, thermally stimulated exoelectron emission or optically stimulated exoelectron emission, respectively.⁷

The goal of the theoretical part of the program was to establish the connection between the electron kinetic processes that occur during laser exposure and exoelectron emission. Bass and Barrett,⁹ Yablonovitch and Bloembergern¹⁰ and Fradin¹¹ have shown that avalanche ionization is the basic mechanism for intrinsic laser damage in alkali halides, glass, quartz, sapphire and other optical materials at frequencies from the ruby frequency down to the near infrared. In their work no consideration was given to lattice defects, e.g., Cl⁻-vacancies in NaCl which form F-centers upon electron capture. These F-centers are traps in the surface layer which are a source of electrons. The kinetic theory of laser induced exoelectron emission has to describe how these traps are

populated during the laser exposure. The mechanism is trapping of free charge carriers. Free carriers (e.g., electrons in the conduction band) are generated by the same processes which, at high photon fluxes, result in dielectric avalanche ionization. Their contribution to the concentration of free carriers depend on the photon flux, the laser frequency and the impurity content of the material. Correlations between high photon flux induced exoelectron emission and laser damage were therefore anticipated.

A phenomenological theory of photon induced electron trapping is presented in Sections 3 and 4. In the case of NaCl, exposed to intense light from a ruby laser, it is shown that multiphoton absorption (or photocarrier generation in general) as well as the presence of F-centers reduces the damage threshold. Avalanche ionization is confirmed to be the dominant damage mechanism in this case. Also, the processes originally suspected of causing TSEE in such materials as alkali-halides may indeed produce characteristic exoelectron images in NaCl. However, careful experiments revealed that a laser produced plasma is a necessary requirement for the type of exoelectron images observed in lithium fluoride.² The experimental results obtained during the program are summarized in Section 5.

SECTION 2

EXOELECTRON EMISSION FROM DIELECTRIC MATERIALS

2.1 GENERAL REMARKS

Thermally stimulated exoelectron emission is defined as the emission of electrons from a given material in a non-steady state at temperatures well below the temperatures at which thermionic electron emission can be detected. Optically stimulated exoelectron emission may be defined in a similar way as the emission of electrons from a given material in a non-steady state at photon energies well below the energies at which conventional photoemission occurs.

Exoelectron emission has been found in a large variety of materials under the following circumstances:⁷

- During or after mechanical deformation of metals
- After exposure of dielectric materials to ionizing radiation and intense laser radiation
- During solidification of metals
- During changes in crystalline structure
- During some chemical or biological reactions

The emission of electrons may occur either spontaneously during or after these processes. Alternatively, it can be stimulated optically or thermally after either mechanical deformation or exposure to ionizing radiation (uv, α -, β -, γ -, x-rays, ions, etc.).

The terminology suggested by Becker⁷ and used in this report is EE for spontaneous exoelectron emission, OSEE for optically stimulated exoelectron emission and TSEE for thermally stimulated exoelectron emission. Naturally, in this work we were interested in dielectric optical materials only. Therefore, we restrict the description of exoelectron phenomena to dielectrics.

A dielectric sample exposed to ionizing radiation will spontaneously emit electrons (EE) for a certain period of time after exposure.

When this emission decays, additional electron emission (TSEE) can be stimulated by further heating of the sample. The latter emission usually shows peaks at various temperatures which are characteristic for a specific material and its surface condition.

A more or less pronounced correlation between exoelectron emission and certain electrical and optical phenomena has been experimentally established for some dielectrics. TSEE in some specimens, for example, exhibits a temperature dependence ("glow curve") that is closely related to thermally stimulated luminescence (TSL) and thermally stimulated conductivity (TSC). Likewise, OSEE has an analog in light stimulated luminescence. Since these effects depend on, or are related to, optical absorption and thermal bleaching;¹³ they should be studied simultaneously in the same sample to shed light on the complex mechanism of exoelectron emission. The importance of both the defect level structure of the surface layer (point defects, impurities, surface states, adsorbed layers of gas, etc.) and the work-function of the solid-gas interface in explaining the features of a particular EE, TSEE, or OSEE curve have become apparent. However, the specific mechanism for the escape of electrons from the surface during such processes is presently not well understood.

Even though EE properties of insulating solids have been, and continue to be, the subject of intensive investigations,⁷ little was known about materials of laser interest at the start of this program; except for the work by Bendix on LiF,³ nothing was reported in the literature on EE from those materials after laser exposure. The exoelectron properties of any of the nonlinear materials or laser glass were unknown as well. Fairly extensive research has been reported on EE after excitation with ionizing radiation on alkali halides, some sulfides, and earth alkaline halides.

Virtually all known alkali halides exhibit thermally-stimulated exoelectron emission (TSEE) or optically stimulated exoelectron emission (OSEE) after exposure to X-rays, short wavelength uv, fast electrons,

and α -, β -, and γ -particles.⁷ Glow peaks have been observed in the range from liquid hydrogen temperatures up to 600°C. Most of the alkali halides emit quite intensely at temperatures above room temperature.

Of all alkali halides, LiF is the most thoroughly studied exoelectron emitter. Bohun¹⁴ and Kramer¹⁵ reported the same single glow peak at about 120°C that we observed after laser exposure.³ Occasionally peaks at higher temperatures were observed by various authors. These peaks are apparently due to different impurities present in the bulk as well as in the surface layer. The main peak at about 120°C has been diagnosed as due to surface centers.⁷ Extensive work has been performed on Mn- and Ti-activated LiF powder, a material of particular interest in applications of EE to radiation dosimetry. However, owing to the scope of this project, we are not interested in intentionally doped materials but rather those which are nominally pure. Of the remaining alkali halides, NaCl, KCl, and KBr have been studied.¹⁶ Glow peaks at 500 to 545°K of all three materials have been found to be due to traps that were identified as F-centers.⁷ Other peaks below room temperature have been found; they are, however, of no interest here because any NDT method for laser surface damage relies on EE peaks above 25°C.

Several alkaline earth halides, namely, CaF_2 , SrF_2 , and BaF_2 are of interest as laser optical materials and have been studied with respect to their exoelectron emission properties. Nominally pure CaF_2 emits usually at around 200 to 240°C.^{17,18} The thermal activation energy of the 240°C peak was determined to be 1.03 eV.¹⁸ BaF_2 exhibits EE peaks at 125°C, 180°C, and 320°C, and the glow peaks of SrF_2 were found to be at 118°C, 253°C, and 383°C.¹⁹

Other high-power laser materials are metal oxides, calcite, ZnS , ZnSe , CdTe , special glasses, and some semi-conductors, as well as compounds used in reflection and anti-reflection coatings. However, except for some results on semiconductors,²⁰ work on these materials is of limited value for our purpose. The reason is that exoelectron emission properties depend to a large extent on the method of preparation and on

impurity content. Since production methods for alkali halides, earth alkaline halides, some metal oxides, and semiconductors are now standardized, fairly reproducible qualities of pure crystals can be readily obtained. This is not the case, however, for most of the other materials considered in this subsection.

Most compounds are expected to be exoelectron emitters. Laser glass, ferroelectric materials, and, most notably, pyroelectric materials play a special role among the complex compounds and are of particular interest in high power laser applications.

2.2 EXOELECTRON MECHANISM

The term "exoelectron emission" is used for charge emission in general from surfaces after excitation (Section 2.1). Magnetic discrimination experiments have shown that not only electrons are emitted but that thermal or optical desorption of negative ions occurs as well (e.g., from X-ray excited ZnO and nominally unexcited MgO and NaCl).⁸ In many cases, however, the emitted charged particles are low energy electrons.⁷ It is fairly well established that the low energy exoelectron escape depth is about 50°A. While the emission of ions must clearly originate in the upper-most adsorption layer of the solid, electrons may originate in energy states characteristic of the bulk material and extending, with some modification, into the surface layer (volume effects) or they may originate in unique surface states (surface effects). Since the basic mechanism of intrinsic bulk and surface damage has been found to be electronic in nature, we will concentrate in this report on the electronic nature of exoelectron emission as well. Desorption of ions, which is important for the theory of exoelectron emission, is a physico-chemical process similar to the evaporation of contaminating material in surface damage. Occasionally field-assisted exoelectron emission is observed and the kinetic energy of the emitted electrons may reach several hundred electron volts.^{21,22}

The theory of thermally stimulated exoelectron emission has to specify the escape mechanism of electrons from the energy levels (traps,

color centers, surface states) in a surface layer with the thickness equal to the escape depth. Obviously, the exoelectron emitter must have a sufficiently low effective work-function (energy difference between the vacuum level and the trap level) to permit the release of electrons from the traps. When this is the case, the so-called Maxwellian tail model adequately describes the exoelectron emission peak.²³

There is, however, evidence from photo-emission experiments and from the measurement of exoelectron energy spectra,²⁴ that, in some cases this model is inadequate. Either the effective work-function is found to be too large or the energy distribution of the electron is non-Maxwellian. To explain these observations, three alternate mechanisms have been suggested:

- Electric Field Assisted Emission

Upon exposing the sample to ionizing radiation, a dipole layer may be formed which subsequently accelerates thermally released, trapped electrons toward and through the surface.²¹ Electric fields of sufficient strength for field emission of electrons may also be generated by changing the temperature of a pyroelectric material such as LiNbO_3 .²²

- Areas of Low Work-Function on the Surface

The effective work-function can be lowered at some points on the surface by adsorbates, impurities, dislocations or grain boundaries. Käämbre interprets the patchy appearance of the BeO -surface, revealed by exoelectron microscopy,⁴ as evidence for this concept.⁸

- Auger-Effect Mechanism²⁵

During the temperature increase or by optical stimulation, holes may be released from hole traps. They can recombine with electrons in other centers and the resulting energy can be transferred to a trapped electron which subsequently is ejected.

Several MgO TSEE peaks coinciding with V_K-center peaks observed in thermoluminescence or bleaching temperatures are taken as evidence for the existence of such a process.²⁶ Energy spectra should, in this case, feature a distinct resonance peak and should not be Maxwellian.

Work on the correlation between laser surface damage and exoelectron emission, reported in the following sections, relies on only one aspect of these exoelectron theories, namely the existence of some type of traps in the surface layer, which can be filled with electrons upon exposure with laser radiation and which can be emptied by either thermal or optical stimulation. Whether the escape process is aided by electric fields or, for that matter, is an Auger-effect is irrelevant.

In the following two sections, we briefly describe the laser damage mechanism and investigate (1) the mechanism of electron trapping during and after laser exposure, (2) the correlations between laser damage and the density of trapped electrons in the surface layer, (3) the role of traps and of the optical and thermal release of trapped electrons in the laser damage, and (4) the influence of multiphoton photocarrier generation on the damage threshold of high quality single crystal sodium chloride.

SECTION 3

LASER INDUCED DAMAGE IN SOLIDS

3.1 THE DAMAGE MECHANISM

Optical damage is defined as an irreversible change of the solid caused by intense light beams.¹¹ Damage may occur in the form of thermal fracture and/or melting. The theory of optical damage has to explain the mechanism by which the energy required for damage is absorbed from the light beam and deposited in the solid.

It is now clearly established that one has to distinguish between two basically different types of damage, namely intrinsic and extrinsic damage. The latter type of damage is usually associated with a lower damage threshold than the former. It is caused by heating of small absorbing inclusions. Intrinsic damage was intensively studied only in the last three years starting with the discovery by Bass and Barrett of the statistical nature of surface damage, which was taken as evidence that the damage mechanism is electron-avalanche breakdown.⁹ Later, Yablonovitch and Bloembergen recognized the importance of avalanche ionization in bulk-damage.¹⁰ Thereafter, the stage was set for much detailed experimental study of various aspects of this damage mechanism in a variety of materials. The work of Fradin, et al.¹¹ helped to clear up many of the remaining problems. As a result of the findings of Crisp and coworkers²⁷ and of Bloembergen,²⁸ the generally lower surface damage threshold can also be explained on the basis of the avalanche-ionization. These authors have shown that both Fresnel reflection and structural defects enhance surface electric fields.

Even though avalanche breakdown appears to be the dominant mode for laser induced damage in most dielectrics in the wavelength region from 0.69μ to 10.6μ , multiphoton absorption becomes increasingly more important at shorter wavelengths.¹¹ We have performed calculations of

the intrinsic damage threshold for NaCl and ruby light where both intrinsic mechanisms are considered. As will be described in Section 4, multiphoton effects tend to lower the damage threshold of NaCl at 0.69μ .

3.2 CORRELATION BETWEEN LASER SURFACE DAMAGE AND EXOELECTRON EMISSION

The generation of heat in the solid in the presence of an electromagnetic wave can be treated classically. Free electrons in the conduction band acquire energy from the alternating electric field (optical field) by the mechanism of inverse Bremsstrahlung²⁹ and the lattice is heated by electron-phonon collisions. The rate of energy deposition to the conduction electrons per unit volume is given by

$$\frac{dW}{dt} = n_c \frac{e^2 \tau_i E^2}{m^* (1 + \tau_i^2 \omega^2)}.$$

where n_c is the density of electrons in the conduction band, e is the electron charge, m^* is the effective electron mass, τ_i is the electron-phonon collision time, E is the rms optical field strength and ω is the laser frequency.

In optical materials which are usually good insulators, n_c is generally quite small ($10^8 - 10^{12} \text{ cm}^{-3}$). At this density very high optical field strengths are required to deposit sufficient energy for damage. However, the optical field itself produces a dramatic increase of n_c via avalanche ionization and multiphoton absorption. This fact is the key to the correlation between exoelectron emission and precursors of the laser damage process. Under the influence of the photon field, electrons are redistributed over higher energy levels of the solid. After the pulse, and in the absence of irreversible damage, the solid returns to thermal equilibrium by various relaxation mechanisms. The population of electrons in impurity levels and in the conduction band decays. Some of the conduction electrons are captured in traps where they remain unless

the temperature is increased again or unless subsequent photons provide the necessary activation energy for their release.

The density of filled traps is a complicated function of the time-dependent laser photon flux and the temperature. In order to understand the relations between trap population and the laser photon flux, time- and temperature-dependent kinetic rate-equations have to be solved. These equations, which are discussed in the next section, represent an extension of the simple model used by the Harvard group.¹¹ In addition to avalanche ionization, the role of multi-photon photocarrier generation and of color centers will be described in detail.

The influence of such factors as impurities, inclusions, contamination and surface imperfections (grooves, pits, scratches, etc.) on n_c and on the temperature T is, of course, not directly amenable to qualitative kinetic calculations. However, any change in n_c and T is reflected as an alteration of the density of filled traps and, therefore, as a change in the exoelectron emission current. The measurement of exoelectrons after exposure of a solid to laser powers up to the surface damage threshold should therefore provide information on precursors of damage in a surface layer of thickness δ , the electron escape depth.

SECTION 4
ELECTRON KINETICS OF INTRINSIC LASER DAMAGE
AND EXOELECTRON EMISSION

4.1 GENERAL FORMALISM

The kinetic theories of intrinsic laser damage in and of exoelectron emission from an insulating solid exposed to intense laser radiation must deal with three distinct phases:

- (1) The exposure of the sample to the laser pulse: The solid interacts with the photon field. Electrons are redistributed over available electron levels by such processes as multiphoton absorption, recombination, trapping, photoemission, avalanche ionization, and thermal transitions. Via inverse Bremsstrahlung and electron-phonon collision, the lattice temperature increases.
- (2) Relaxation: The lifetime of an excited electron is generally longer than the laser pulse width. Relaxation continues after the laser-pulse. A small number of electrons are trapped in metastable levels. Only those traps that are in a thin surface layer have to be considered for exoelectron studies. The spatial distribution of the trapped electrons is a map of the spatial distribution of the conduction electrons which were generated during the laser pulse. The temperature distribution, imprinted onto the solid by the processes above, diffuses and the solid eventually returns to ambient temperature.
- (3) Subsequent heating of the exposed sample (thermally-stimulated exoelectron emission): The probability for thermal release of the trapped electrons increases with increasing temperature. A small portion of the electrons released from the traps overcomes the work function barrier and is emitted as exoelectrons into the vacuum.

The theory has to provide the link between the processes occurring during the time of the laser exposure and the spatial intensity distribution of the exoelectron emission. At high laser power densities below the surface damage threshold, these processes are identical to processes leading to laser surface damage. Since the processes occurring during the laser exposure also affect the spatial distribution of trapped electrons, the investigation of exoelectron emission after exposure of the sample to intense laser light below the surface damage threshold may shed light on the mechanism of laser breakdown of transparent material.

The task of analyzing the various processes has been simplified considerably owing to recently published quantitative work on multiphoton excitation of conduction electrons³⁰ and on the nature of laser breakdown in alkali halides,¹¹ one of the more important classes of materials to be considered in this research project. Multiphoton absorption and avalanche ionization are the main sources of conduction electrons during the duration of the laser pulse. In addition, it is now established that the theory of dc dielectric breakdown³¹ of these materials is applicable without major modification to optical fields.¹⁰

In the following, we will use an electron kinetics approach to describe the spatio-temporal behavior of the density of conduction electrons in the three experimental phases described above. Rate equations of the type to be discussed here can be found in an article by Franz.³¹ In the simplest case, the energy levels of an insulating solid are described by a band model. For thermal equilibrium and in the absence of radiation, the electrons occupy the completely filled valence band. All trap levels and the conduction band can be assumed to be empty. Denoting the concentration of conduction electrons as n_c , the concentration of trapped electrons in N_t traps as n_t , and the concentration of electrons

in the valence band as n_v , and neglecting diffusion of electrons, we write,

$$\frac{dn_c}{dt} = n_c \omega_i + n_v \omega_{vc} + n_t \omega_{tc} - n_c (n_c + n_t) \omega_{cv} - n_c (N_t - n_t) \omega_{ct} \quad (2)$$

$$\frac{dn_t}{dt} = n_v (N_t - n_t) \omega_{vt} + n_c (N - n_t) \omega_{ct} - n_t (n_c + n_t) \omega_{tv} - n_t \omega_{tc} \quad (3)$$

where the ω_{ik} 's are the transition probabilities in appropriate units (see below). The subscripts c, v and t for conduction band, valence band and traps respectively designate the transitions (e.g., ω_{cv} is the transition probability for an electron in the conduction band to reach the valence band, etc.); ω_i is the avalanche ionization probability. All electron concentrations and transition probabilities are functions of the coordinates z (along the axis of the laser beam and perpendicular to the entry surface of the sample), r (the radial distance from the beam axis), and time t.

Only traps in a surface layer of thickness δ (escape depth of the exoelectrons) participate in the formation of the spatial distribution of filled traps. The goal of the theory is therefore to calculate $n_t(t_p, r)$ where t_p is the time duration of the laser pulse. To do this, we must know the transition probabilities ω_{ik} , all of which depend on the spatio-temporal characteristics of the laser beam. Furthermore, the temperature T of the sample enters as an important parameter and it, too, is a function of r, z, and t.

Field emission or tunneling of electrons from the valence-band or impurity levels and traps, an important process in the theory of dc-dielectric breakdown, is replaced by multiphoton transitions at electric fields of optical frequencies.^{11,32}

Several of the transition rates ω_{ik} in equations (2) and (3) contain contributions from optical transitions and thermal transitions.

Using the superscripts "o" and "th" to distinguish these processes, the transition rates from the traps to the conduction band³¹ are

$$\omega_{tc} = \omega_{tc}^{th} + \omega_{tc}^o \quad (4)$$

with

$$\omega_{tc}^{th} = 2 \omega_{ct} \left(\frac{m^* k T}{2} \right)^{3/2} \exp(-E_t/k T) \quad (5)$$

where E_t is the trap depth, m^* is the effective electron mass at the lower edge of the conduction band, and ω_{ct} is the rate of trapping conduction electrons in the traps. Since, in our case, the traps are expected to be at most 2 eV below the lower edge of the conduction band, the energy difference between the upper edge of the valence band and the traps is large in wide-band-gap materials such as alkali halides. We may therefore safely neglect the thermal contributions to the transition rates ω_{vc} and ω_{vt} . The rate of multiphoton transitions of valence electrons to the conduction band is given by

$$\omega_{vc} = \sigma_N F^N \quad (6)$$

where σ_N is the cross section for N-photon absorption, measured in $\text{cm}^{2N} \text{sec}^{N-1}$, and F is the laser photon flux. The transition rate ω_{cv} is determined by the known lifetime of free electrons.

Yablonovitch's solution¹⁰ of the electron kinetic balance equations is easily obtained if one neglects trapping and multiphoton effects and retains only the avalanche term in equation (2):

$$n_c(t_p) = n_c(0) \exp \left(\int_0^{t_p} \omega_i dt \right) \quad (7)$$

4.2 APPLICATION TO INTRINSIC DAMAGE INDUCED BY RUBY LASER RADIATION IN SODIUM CHLORIDE

4.2.1 Rate Equations

NaCl was chosen because its properties are well known³³ and the cross sections for multiphoton absorption and electron trapping, the avalanche ionization rate, transition probabilities, etc., are either known from independent experiments or can be calculated. We consider a pure NaCl crystal containing a given density of negative ion-vacancies. The natural density of ion-vacancies in NaCl at 100°C is on the order of $3 \times 10^5 \text{ cm}^{-3}$, which represents the lowest obtainable theoretical density. Real crystals contain at least $1 \times 10^{16} \text{ Cl}^-$ - vacancies (traps) which form F-centers upon capture of a free electron.³³ Positive ion vacancies may act as recombination centers for free electrons thereby influencing the lifetime of free carriers. We use experimentally determined free-electron lifetimes and thus take the effect of positive ion-vacancies into account. These vacancies also effect the electron kinetics in another way, namely, by providing real intermediate electron levels for multiphoton absorption and cascade photon absorption. In both cases, the cross section for photocarrier generation increases. We discuss this question later.

Multiphoton cross sections measured by Catalano, et al.³⁰ are presently considered to be too large by some workers.³⁴ Therefore, it was necessary to study all damage and exoelectron phenomena for a range of cross sections. Since the wavelength ($\lambda = 6943 \text{ \AA}$) of the ruby laser corresponds to a quantum energy of 1.78 eV and NaCl has a band gap of $E_g = 8.1 \text{ eV}$, a five-photon absorption process is required for free carrier generation.

The physical processes leading to population of electron traps in NaCl after laser exposure can be described by equations (2) and (3) after some appropriate modifications. A schematic energy level diagram for NaCl containing F-centers is shown in Figure 1.

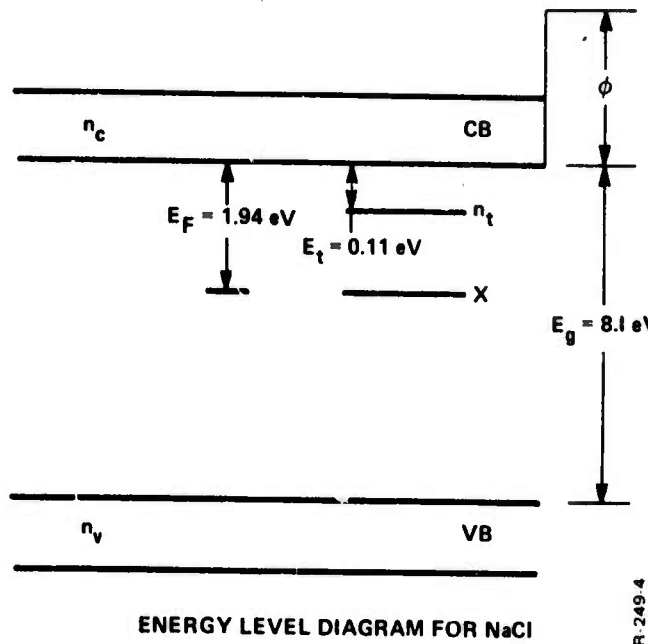


Figure 1 - Schematic energy level diagram of NaCl.

The modifications of equations (2) and (3) are:

- (1) In addition to the ground level of the F-center, we must consider an excited level. According to Markham,³³ the trapping traffic toward the ground state flows via the excited level. Transitions between the levels and the conduction band are possible with thermal activation energies of 1.94 eV and 0.11 eV, respectively. The optical activation energy³³ of the ground level is 2.75 eV, which requires a two-photon absorption process at the ruby wavelength.
- (2) We replace the term $(n_c + n_t)\omega_{cv}$ in equation (2) by the lifetime $\tau_c = 10^{-6} \text{ sec}$ as measured by Catalano et al.³³
- (3) The transition probabilities ω_{vt} and ω_{tv} are sufficiently small to be neglected.

- (4) A third equation for the change in temperature during the laser exposure is added. The diffusion of the temperature profile, imprinted onto the sample by the TEM_{00} mode laser intensity profile, is discussed in Section 4.2.8.

The relevant rate equations to be solved are now:

$$\frac{dn_c}{dt} = n_v \omega_{vc} - n_c / \tau_c + n_t \omega_{tc} - n_c (N_t - X - n_t) \omega_{ct} + \omega_{Fc} X + \omega_i n_c \quad (8)$$

$$\frac{dn_t}{dt} = -n_t \omega_{tc} + n_c (N_t - X - n_t) \omega_{ct} - n_t / \tau_t \quad (9)$$

$$\frac{dX}{dt} = -\omega_{Fc} X + n_t / \tau_t \quad (10)$$

and

$$\frac{dT}{dt} = (\rho \kappa)^{-1} \frac{dW}{dt} \quad (11)$$

We used the following notation:

N_t = density of Cl^- vacancies

X = density of F-centers in ground state

n_r = refractive index

n_t = density of F-centers in excited state

n_c = density of free electrons in the conduction band

n_v = density of valence electrons

ω_i = avalanche ionization rate

ω_{vc} = transition rate for 5-photon photocarrier generation
 ω_{ct} = transition rate for electron capture into the excited
 F-center level
 ω_{tc} = transition rate for electrons to go from the excited
 F-center level to the conduction band
 $\tau_c = 10^{-6}$ sec, lifetime of conduction electrons³⁰
 N_c = density of states in the conduction band cb
 $\tau_t = 10^{-6}$ sec, lifetime of electrons in excited F-center
 levels³³
 ω_{Fc} = transition rate for electrons to go from the ground
 level of the F-center to the conduction band
 T = temperature
 W = absorbed energy density
 ρ = density of crystal
 κ = specific heat of the crystal
 t_p = total laser pulse length
 $\tau_i =$ electron-photon collision time $\approx 0.5 \times 10^{-15}$ sec
 $\Delta\omega$ = width of F-band ≈ 0.46 eV
 t = time
 E_{tr} = trap depth (in general)
 F = laser photon flux
 A^* = laser peak flux
 $E_g = 8.1$ eV, bandgap of NaCl
 $E_F = 1.94$ eV; "thermal" energy difference between F-center ground
 level and lower edge of the conduction band in NaCl³³
 $E_t = 0.11$ eV; energy difference between excited level of F-center
 and lower edge of the conduction band in NaCl³³
 $\lambda = 6943 \text{ \AA}$; wavelength of ruby light
 $\omega = 2\pi\nu$
 $\nu = \frac{\omega}{2\pi} = (2\pi)^{-1} \times 2.63 \times 10^{15} \text{ s}^{-1}$; frequency of ruby laser
 light (the corresponding quantum energy is 1.78 eV)
 r = distance from center of the laser beam

σ_5 = cross section for five-photon absorption in NaCl
 σ_1 = cross section for single-photon absorption by an electron in the excited level of an F-center
 σ_2 = two-photon absorption cross section for ground state F-center
 σ_F = cross section for electron capture into ground level of F-center
 σ_t = cross section for electron capture into excited level of F-center
E = rms field strength of laser photon field
f = oscillator strength
 v_{th} = thermal velocity of free electrons
c = speed of light
D = difficulty

4.2.2 Photon Induced Transition Rates

The photons of the ruby laser generate photocarriers via five-photon absorption of valence electrons, two-photon absorption of electrons in the ground level of the F-center, and single-photon absorption of electrons in the excited F-center level.

The five-photon generation rate is found to be $n_v \omega_{vc} = n_v \sigma_5 F^5 = 1.12 \times 10^{-118} F^5 \text{ sec}^{-1}$, based on $n_v = 2.23 \times 10^{22} \text{ cm}^{-3}$ for the density of valence electrons and on the smallest published value³⁰ of $\sigma_5 = 0.5 \times 10^{-140} \text{ cm}^{10} \text{ sec}^4$ for the cross section. Even though the value for σ_5 agrees reasonably well with theoretical estimates, Fradin³⁴ contends that it is too high because Catalano, et al.³⁰ do not adequately characterize their laser beam and conceivably used a multi-transverse mode laser beam. It is well known that multiphoton cross sections, experimentally determined with multi-mode laser beams, are too large. We therefore performed calculations with the smaller value, $\sigma_5 = 0.5 \times 10^{-141} \text{ cm}^{10} \text{ sec}^4$ as well. As it turned out, the intrinsic damage threshold for nanosecond laser pulses increased slightly when σ_5 is reduced by a factor of 10 (see Section 4.2.6).

The transition rate for single photon absorption by excited F-centers is given by $\omega_{tc}^0 = \sigma_1 F$. We can estimate σ_1 from Smakula's formula:³³

$$\sigma_1 \leq \frac{2}{9} \frac{e^2}{m^* c} \frac{f}{\Delta\omega} \frac{(2 + n_r^2)^2}{n_r} \approx 1 \times 10^{-16} \text{ cm}^2 \quad (12)$$

For the calculations we have used $\sigma_1 \leq 10^{-16} \text{ cm}^2$ which might be too large by two orders of magnitude. However, this is of no consequence for the calculations of intrinsic damage or the trap distribution. The excited F-center is thermally very strongly coupled to the conduction band. This coupling, as it turns out, is the process which determines n_t .

In a similar way, we calculated the cross section σ_2 for the two-photon transition from the ground state of the F-center to the conduction band. According to Kleinman³⁵ the optical contribution to ω_{Fc}^0 is

$$\omega_{Fc}^0 = \sigma_2 F = \frac{r_0^2 8\pi^3 c^2 f^2}{n_r^2 \omega^2 \Delta\omega} F^2 \quad (13)$$

Here $r_0 = 2.82 \times 10^{-13} \text{ cm}$ is the classical electron radius, c is the velocity of light, ω (ruby) = $2.63 \times 10^{15} \text{ s}^{-1}$, and f is an average of the involved oscillator strengths.

With $\Delta\omega \approx 0.46 \text{ eV} \approx 0.68 \times 10^{15} \text{ s}^{-1}$ and $f \approx 1$, we obtain $\omega_{Fc}^0 \approx 1.6 \times 10^{-48} F^2 (\text{s}^{-1})$.

4.2.3 The Avalanche Ionization Rate

The rate of avalanche ionization ω_i is a function of the rms optical field strength E or the laser flux. Yablonovitch and Bloembergen have calculated $\omega_i(E)$ for optical fields using previously published data of dc fields in thin NaCl samples.³⁶ Fradin, et al, have used their data for a calculation of the breakdown rms field as a function of the laser pulse width.¹² However, the experimental data could be fitted only by shifting Yablonovitch's $\omega_i(E)$ -curve to higher fields.

Since Fradin's results are plotted on a double-logarithmic scale, we found it convenient to express the numerical values as follows:

$$\log \omega_1(E) = 8.17 + 4.22 \log E - 0.823 (\log E)^2 \quad (14)$$

The values for $\omega_1(E)$ in sec^{-1} are obtained from equation (14) by using E in MV/cm . Equation (14) is a very good approximation for $1 \leq E \leq 50$ (MV/cm). We note that the theoretical expression¹¹ $\omega_1(E) \propto \exp(-K/E)$ may be obtained from equation (14) in a first approximation. However, Yablonovitch's curve,¹⁰ shifted as described above, cannot be fitted quite as well with this exponential curve.

4.2.4 Thermal Transition Rates

The thermal transition probabilities ω_{tc}^{th} and ω_{Fc}^{th} are related to the cross sections σ_t and σ_F for capture of free electrons in the excited and ground level of the F-center.³³ Both depend, of course, on the energy E_t and E_F , respectively:

$$\omega_{tc}^{\text{th}} = v_{th} N_c \sigma_t \exp(-E_t/kT) \quad (15)$$

$$\omega_{Fc}^{\text{th}} = v_{th} N_c \sigma_F \exp(-E_F/kT) \quad (16)$$

where $v_{th} = (3 kT/m^*)^{1/2}$ and $N_c = 4.8 \times 10^{17} \text{ T}^{3/2} \text{ cm}^{-3}$. According to Markhan,³³ electron capture by Cl^- - vacancies occurs via the excited level with a cross section $\sigma_t \approx 10^{-13} \text{ cm}^2$. Thereafter, the ground level is reached by relaxation with a relaxation time $\tau_t = 10^{-6} \text{ sec}$.

From equation (15) we find with $v_{th} \approx 1.45 \times 10^7 \text{ cm sec}^{-1}$ (temperature dependence neglected) $\omega_{tc}^{\text{th}} \approx 7 \times 10^9 \text{ T}^{3/2} \exp(-0.11 \text{ eV/kT})$ and, since $\omega_{ct} = v_{th} \sigma_t$ we have $\omega_{ct} = 1.45 \times 10^{-6} (\text{cm}^3 \text{ sec}^{-1})$.

The thermal transition probability ω_{Fc}^{th} can only be estimated. We know³³ that $\sigma_F \leq 10^{-1} \times \sigma_t$. It decreases with temperature. We assume, fully aware of the approximation, that $\omega_{Fc}^{th} \approx 7 \times 10^8 T^{3/2} \exp(-E_F/kT)$. These transitions, as we will see, have little influence on the damage process. They are, however, important in the exoelectron processes. Since we do not intend to calibrate absolute exoelectron emission intensities versus laser flux, the qualitative description of the thermal transition probabilities suffices. We could have treated this whole question somewhat differently. Since ω_{tc}^{th} , ω_{tc} , τ_t , and therefore n_t , are known fairly accurately, the population of F-centers in the ground state can be calculated from Boltzmann statistics, under the assumption of steady-state thermal equilibrium.

4.2.5 Numerical Calculations - General Remarks

Solution of equations (8) through (11) were obtained numerically by a modified Runge-Kutta method with variable step size and precision. Due to the fortunate circumstance that all relaxation times involved are much longer than the laser pulse length $\tau_p \leq 60$ nsec, we can separate the calculations of phase (1) and (2) (see Section 4.1). For phase (1), we neglect all terms proportional to τ_t and τ_c and calculate the relevant population densities n_c , n_t , and X , as well as the sample temperature, as a function of photon flux at various times during the laser pulse. Electron diffusion and thermal diffusivity can be neglected in this time domain.

The second phase, which involves no photons, describes the redistribution of the electrons due to relaxation to a steady-state equilibrium. In this time domain ($\tau > 10^{-6}$ sec), we have to consider diffusion of electrons as well as temperature diffusion. The heat generated at high laser peak powers in the center of the laser intensity distribution bleaches F-centers. In this way the heat influences the spatial distribution of the trapped electrons and, therefore, the spatial distribution of the exoelectron emission intensity.

The last phase, namely, the thermal stimulation of exo-electron emission, is based on the thermal transition characterized by ω_{Fc}^{th} . The probability for trapped electrons to reach the conduction band increases with temperature. Most of these electrons recombine with holes remaining in recombination centers or the valence band after the laser exposure. A small fraction of electrons leave the solid as exoelectrons. As the traps empty, the rate of the recombination and the emission decreases until thermal equilibrium is restored.²³

4.2.6 Generation of Free Carriers and Damage Mechanism in NaCl

We first discuss the various processes that produce free carriers. In Fradin's and Bloembergen's^{10,11} calculations, an initial concentration of $n_c(0) = 10^{10} \text{ cm}^{-3}$ is assumed. Due to avalanche ionization, this density increases. The authors suggest that breakdown occurs at $n_c = 10^{18} \text{ cm}^{-3}$ at which point the lattice temperature reaches several hundred degrees centigrade in a 60-nanosecond laser pulse.

We are interested in the contributions of multiphoton effects and lattice defects to the generation of free carriers and to the damage process. Therefore, we have calculated n_c at the peak of the laser pulse ($t = t_p/2$) and at end of it ($t = t_p$) for various pulse lengths as a function of the peak laser flux A^* . The laser pulse shape is expressed by

$$F(t) = A^* \sin^2(\pi t/t_p) \quad (17)$$

in reasonable approximation to measured laser pulse shapes.

In Figure 2, the concentration of free electrons reached at the end of the laser pulse is shown as a function of the peak flux for a 60 nsec pulse (30 nsec FWHM). The avalanche mechanism is compared with the five-photon mechanism in the presence of $5 \times 10^{-16} \text{ Cl}^-$ vacancies per cm^3 . The peak flux A^* required to reach the "damaging" concentration $n_c = 10^{18} \text{ cm}^{-3}$ at the end of the pulse is listed in Table I for the different processes. Multiphoton processes alone cannot damage NaCl.

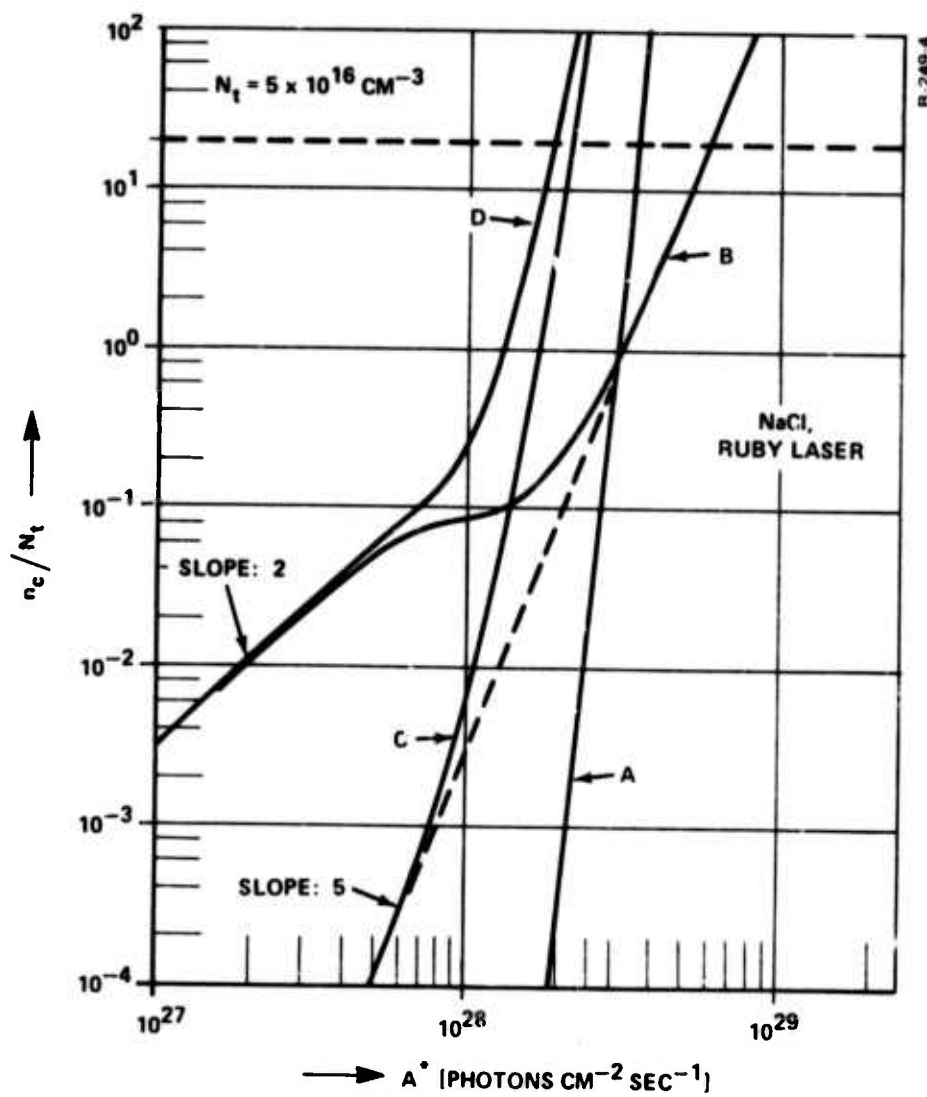


Figure 2 - Normalized concentration n_c/N_t of free electrons in NaCl containing $5 \times 10^{16} \text{ Cl}^-$ -vacancies as a function of laser peak flux A^* for 60 nsec ruby laser pulses.

Compared are different mechanisms.

- A. Avalanche Ionization, ω_i from equation (14),
 $n_c(0) = 10^{10} \text{ cm}^{-3}$, no traps
- B. Multiphoton absorption only, $\sigma_5 = 0.5 \times 10^{-140} \text{ cm}^{10} \text{ sec}^4$, $5 \times 10^{15} \text{ cm}^{-3}$ filled traps
- C. Multiphoton and avalanche, $5 \times 10^{16} \text{ cm}^{-3}$ initially empty traps
- D. Multiphoton and avalanche, $5 \times 10^{15} \text{ cm}^{-3}$ initially filled traps

The "damaging" concentration $n_c = 10^{18} \text{ cm}^{-3}$ is indicated by the dashed horizontal line (see Table I).

Table I - The peak flux A^* of a 60 nsec ruby laser pulse required to produce a damaging concentration of $n_c = 10^{18} \text{ cm}^{-3}$ of free carriers in NaCl at the end of the pulse.
 Comparison of different mechanisms.

R-2494

Mechanism	$A^*(10^{28} \text{ cm}^{-2} \text{ sec}^{-1})$	Ratio $A^*/A^*(\text{Avalanche})$
1. Avalanche: $n_c(0) = 10^{10} \text{ cm}^{-3}$	3.4	1
2. Multiphoton: $5 \times 10^{15} \text{ cm}^{-3}$ filled traps	5.9	1.73
3. Avalanche + Multiphoton: $5 \times 10^{16} \text{ cm}^{-3}$ empty traps	2.2	0.64
4. Avalanche + Multiphoton: 5×10^{15} filled traps	1.8	0.53

Above $A^* = 3 \times 10^{28}$ photons per sec and cm^2 the avalanche mechanism is far more efficient. However, the combined effects of multiphoton and avalanche carrier generation produce breakdown at a peak flux which is about half that required when avalanche ionization alone is present. The initial trap population has a small effect on the damage threshold up to a concentration of 5×10^{15} F-centers (filled traps). This F-center density corresponds to an absorption coefficient $\alpha = 0.68 \text{ cm}^{-1}$ at the absorption peak; that is, the crystal is noticeably discolored. The damage threshold is expected to decrease measurably with increasing density of F-centers.

Let us discuss the curves in Figure 2 somewhat further. Curves B and D start with a slope of two. This is caused by the two-photon absorption of F-centers. The supply of electrons from F-centers is exhausted at peak fluxes around $1 \times 10^{28} \text{ cm}^{-2} \text{ sec}^{-1}$, leading to a concentration of free carriers equal to the initial concentration of F-centers. Multiphoton absorption begins to contribute to n_c at about $A^* = 1.5 \times 10^{28} \text{ cm}^{-2} \text{ sec}^{-1}$ and, in the absence of avalanche ionization, would dominate at $A^* = 3 \times 10^{28} \text{ cm}^{-2} \text{ sec}^{-1}$. (Note slope of 5 for curve B.)

The generation of free carriers by avalanche ionization is calculated from Eqs. (7) and (14) and plotted versus the peak flux in curve A. We used Fradin's value of 10^{10} cm^{-3} for the initial concentration of electrons in the conduction band. At $A^* = 2 \times 10^{28} \text{ cm}^{-2} \text{ sec}^{-1}$, this process has produced about 5×10^{12} free carrier per cm^3 . The "damaging" concentration of 10^{18} cm^{-3} is reached at $A^* = 3.4 \times 10^{28} \text{ cm}^{-2} \text{ sec}^{-1}$. By comparing curves C and D with A, it is immediately obvious that multiphoton absorption and the release of trapped electrons by two-photon absorption provide a concentration of free electrons at the onset of avalanche (at $A^* \approx 1 \times 10^{28} \text{ cm}^{-2} \text{ sec}^{-1}$) which is many orders of magnitudes larger than the concentration provided at that flux by avalanche ionization alone. This fact is, in effect, responsible for the lower intrinsic laser damage threshold.

The influence of the suspected error in the multiphoton cross section σ_5 on the damage threshold is shown in Figure 3. The concentration n_c reached at the end of the laser pulse at $t = t_p$ is plotted as a function of the peak flux A^* for a number of different laser pulse lengths t_p . The dashed curves were obtained with a cross section which is 10 times smaller. The damage threshold is slightly larger for the smaller cross section at $t_p \geq 1 \times 10^{-8}$ sec. This result is not surprising if one considers that, for a given laser pulse, the total free electron density generated by five-photon absorption scales with $\sigma_5 F^5$. Five-photon absorption would only be negligible if σ_5 , determined by Catalano et al.,³⁰ would be as much as 3 orders of magnitude too large. Reliable experimental data for σ_5 are required. In this connection, it is important to point out that the argument that Catalano's value for σ_5 is too large may well be justified.³⁴ However, in a real crystal, a number of mechanisms conceivably contribute to additional photocarrier generation. In particular, absorption via real intermediate impurity levels can increase the rate of photocarrier generation. Experiments on the frequency dependence of the intrinsic laser damage threshold in alkali halides indicate, on the other hand, that below the ruby frequency the dominant mechanism is indeed avalanche ionization.¹¹

We now consider the definition of the damage threshold and its dependence on the length of the laser pulse. It is noted that the kinetic approach of this investigation does not take into account the statistical aspects discovered by Bass and Barrett.⁹ Statistical variations of the damage probability and the time at which damage occurs during the laser pulse depend on the size of the focal volume¹¹ and become less important as the focal volume increases. Boling does not observe breakdown statistics in Nd-2 glass with his 1.5 to 2 mm diameter minimum laser spot size.³⁷ Consequently, we are dealing with fairly well-defined damage thresholds and it is therefore important to define breakdown criteria. The Harvard group is not specific as far as the definition

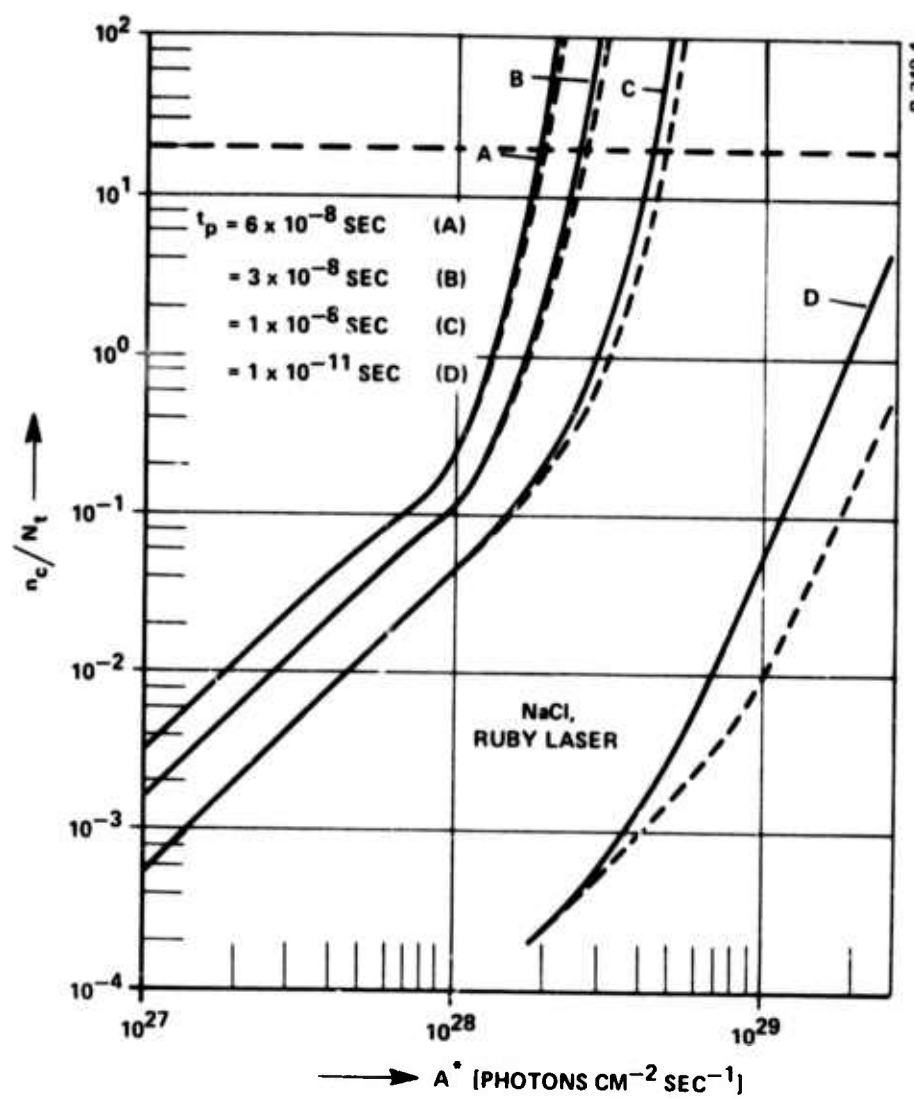


Figure 3 - Normalized concentration n_e/N_t of free electrons in NaCl containing $5 \times 10^{-3} \text{ cm}^{-3}$ Cl^- -vacancies as a function of laser peak flux A^* for ruby laser pulses of several different pulse lengths t_p .

$$\text{Solid lines: } \sigma_5 = 0.5 \times 10^{-140} \text{ cm}^{10} \text{ sec}^4$$

$$\text{Dashed lines: } \sigma_5 = 0.5 \times 10^{-141} \text{ cm}^{10} \text{ sec}^4$$

$$\text{Initial F-center concentration: } 5 \times 10^{15} \text{ cm}^{-3}$$

of intrinsic breakdown is concerned.³⁸ In several publications, breakdown is assumed to occur at a free carrier generation of $1 \times 10^{18} \text{ cm}^{-3}$. On other occasions,¹¹ damage is said to occur when the solid melts. In our investigations, we found that these two definitions of breakdown are in effect not identical regardless of whether the damage mechanism is a pure avalanche process or is aided by photocarrier generation. A concentration of free carriers larger than $1 \times 10^{18} \text{ cm}^{-3}$ is required if damage occurs at the melting point of NaCl ($T = 1074^\circ\text{K}$). The difference is quite large for short laser pulse lengths. The peak flux of a damaging pulse may be as much as a factor 3 larger for picosecond laser pulses (Table II). We based these calculations on a NaCl crystal containing $N_t = 5 \times 10^{16} \text{ Cl}^-$ vacancies of which 10% are initially filled with electrons (called standard sample from here on). However, similar results are obtained for all other conditions considered in this report (e.g., empty traps, no contribution of photocarrier generation, very small Cl^- -vacancy concentration, etc.).

A comparison of the two different definitions of the intrinsic laser damage threshold, the concentration defined and the temperature defined thresholds, is made in Figure 4. The peak ruby photon flux A^* required for damage is shown as a function of laser pulse length t_p . We have plotted $\log (1/t_p)$ vs $A^{*-1/2}$. In this form a straight line with a negative slope is expected when the ionization rate is given by⁹

$$\omega_i(E) \propto \exp(-K/E)$$

instead of Eq. (14). Again, the curves of Figure 4 were calculated for a NaCl standard sample. The computer calculations for the damaging peak flux A^* were performed so that the damaging concentration $n_c = 10^{18} \text{ cm}^{-3}$ or the temperature $T = 1074^\circ\text{K}$ were reached at the end of the laser pulse at $t = t_p$. Different values for A^* , the peak flux of the damaging pulse, are obtained if one specifies damage to occur at a time $t < t_p$. This brings up the important question: At what time during the laser pulse does damage occur? We return to this problem shortly. For now we just note that in the classic work by Bass and Barrett³⁹ and Fradin,¹¹ the most probable time for damage to occur is shortly before the time at which F reaches the peak flux A^* .

Table II - Definition of damage threshold. The ratio R of the peak power A^* , required for T to reach the melting point of NaCl at the end of the pulse, to A^* required for n_c to reach 10^{18} cm^{-3} at the same time, is listed in column 2 for various laser pulse lengths. Column 3 lists the concentration of free carriers at the melting point.

t_p [sec]	R	n_c ($T = 1074^\circ\text{K}$) [10^{18} cm^{-3}]
1×10^{-11}	2.91	314.8
3×10^{-11}	2.47	175.3
1×10^{-10}	2.05	98.6
3×10^{-10}	1.74	51.1
1×10^{-9}	1.48	36.5
3×10^{-9}	1.33	22.6
1×10^{-8}	1.22	12.8
3×10^{-8}	1.16	7.3

R-249-4

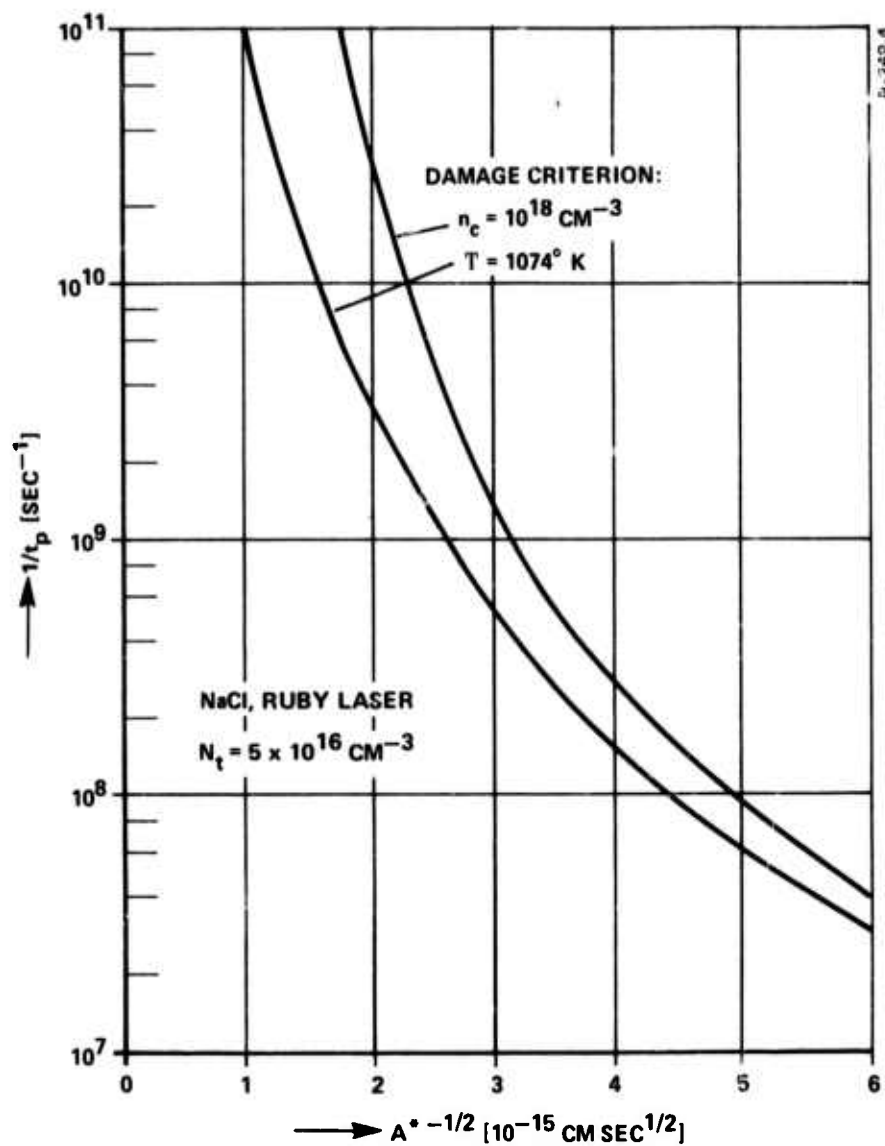


Figure 4 - Pulse length dependence of the peak ruby laser flux required to induce intrinsic damage in NaCl at the end of the laser pulse.

Calculated with $N_t = 10^{16} \text{ cm}^{-3}$, $X(0) = 5 \times 10^{15} \text{ cm}^{-3}$ (standard sample), ω_1 from equation (14) and $\sigma_5 = 0.5 \times 10^{-140} \text{ cm}^{10} \text{ sec}^4$. Two definitions of the damage threshold are used

- concentration-defined threshold
- temperature-defined threshold

The laser pulse width dependence of the damage threshold was therefore recalculated for the case that the damaging flux is reached at the peak of the laser flux at $t = t_p/2$. The result is shown in Figure 5, where we compare three different mechanisms. Curve A is the case where avalanche ionization alone produces damage and the ionization coefficient from Eq. (14) is used. Curves B and C contain the multiphoton and trap contributions. We have chosen the smaller cross section $\sigma_5 = 0.5 \times 10^{-141} \text{ cm}^{10} \text{ sec}^4$. In both cases 10% of the $5 \times 10^{10} \text{ Cl}^-$ vacancies were filled at $t = 0$. The differences in the two curves is simply the time at which damage occurs. The dashed line is obtained with $\omega_i(E) \propto \exp(-K/E)$. Experimental data from Fradin, et al.³⁸ are included as well. We have shifted Fradin's curve along the horizontal axis to obtain a good fit at $t_p = 10^{-11} \text{ sec}$. A similar fit may be obtained with curve A. The computed pulse width dependence of the intrinsic damage threshold is in remarkable agreement with experimental data for laser pulses having a total length $t_p \leq 10^{-8} \text{ sec}$.

Shifting curves as in Figure 5 may be justified for comparison of the shape. However, the absolute values of the damage threshold, are of interest also. Therefore, we have compiled a list of damage thresholds that were measured or computed for different damage mechanisms in NaCl at the ruby frequency. The results are given in Table III. At long pulse durations, the experimental and computed results are in good agreement for all cases. Some discrepancies become apparent at shorter pulse lengths where the fit of ω_i from Eq. (14) with the experimental data³⁸ is not as good. The experimentally determined intrinsic damage thresholds are somewhat smaller than the ones predicted by Yablonovitch¹⁰ (see Section 4.2.3).

We now return to the question of the occurrence of intrinsic damage during the laser pulse. It is instructive to compute the time dependence of the free carrier concentration and of the temperature in the focal volume. The results for a 60 nsec ruby pulse impinging on the standard NaCl crystal are shown in Figure 6. We considered a case where

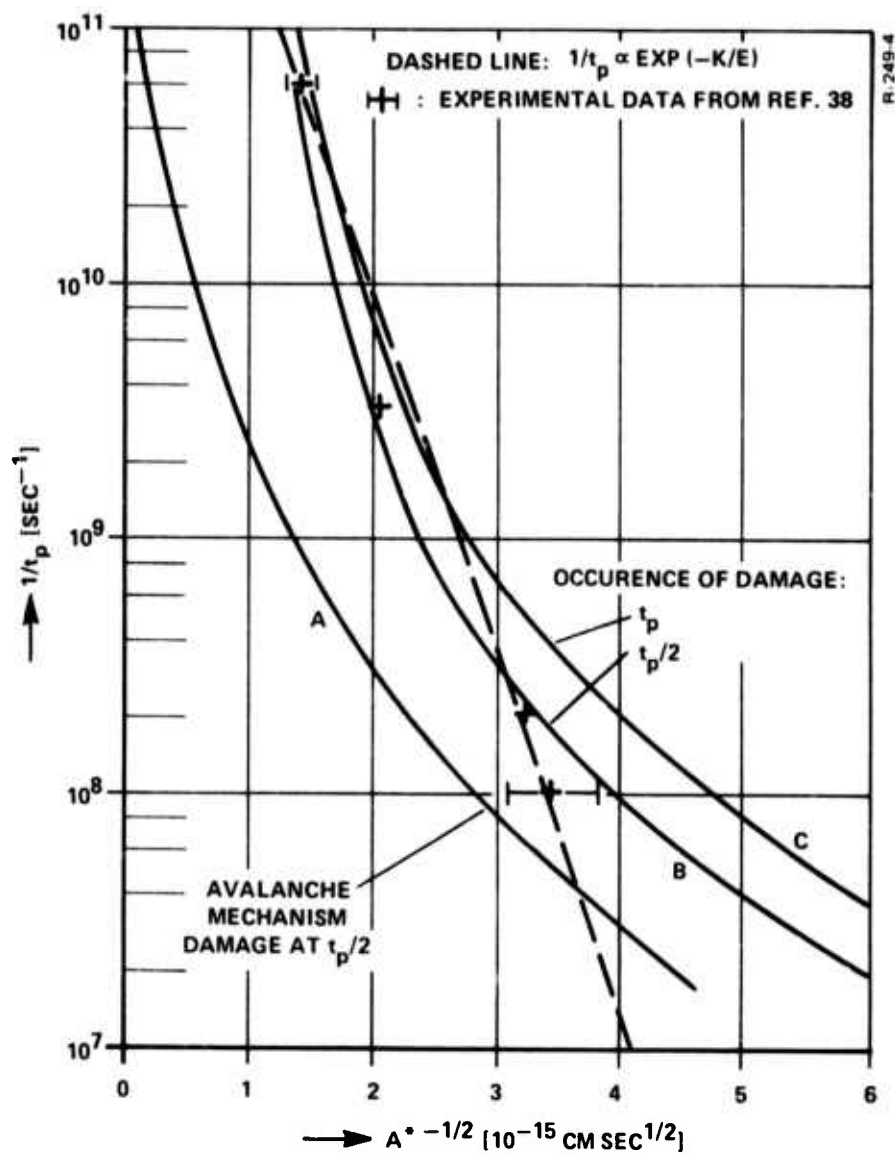


Figure 5 - Dependence of the intrinsic damage threshold on the ruby laser pulse duration for NaCl; damage criterion: $n_c = 1 \times 10^{18} \text{ cm}^{-3}$

A. Avalanche ionization only [ω_i from equation (14)], damage at $t = t_p/2$

B. Avalanche and multiphoton, damage occurs at $t = t_p/2$

C. Avalanche and multiphoton, damage occurs at $t = t_p$

For B and C: $\sigma_5 = 0.5 \times 10^{-141} \text{ cm}^{10} \text{ sec}^4$, standard sample

Note: The experimental data were obtained at the Nd-frequency, however, the results for the ruby frequency are practically identical.⁴⁰

Table III - Comparison of measured and calculated damage thresholds for NaCl at the ruby frequency.

	$t_p = 300 \text{ psec pulse}$	$t_p = 10 \text{ nsec pulse}$
Flux, rms electric field	$A* [10^{29} \text{ cm}^{-2} \text{ sec}^{-1}]$	$A* [10^{29} \text{ cm}^{-2} \text{ sec}^{-1}]$
Experiment: (11) Nd or ruby (FWHP pulse length)		$E_{\text{rms}} [\text{MV/cm}]$
Avalanche:		$E_{\text{rms}} [\text{MV/cm}]$
$n_c = 10^{18} \text{ cm}^{-3}$ reached at $t_p/2$	11.5	9.0
t_p	7.1	7.0
Multiphoton assisted avalanche: $5 \times 10^{-15} \text{ cm}^{-3}$ initial F-centers		
1. Large σ_5		
$n_c = 10^{18} \text{ cm}^{-3}$ at $t_p/2$	1.46	3.2
$n_c = 10^{18} \text{ cm}^{-3}$ at t_p	1.43	3.1
$T = 1074^\circ\text{K}$ at t_p	2.48	4.3
$T = 1074^\circ\text{K}$ at $t_p/2$	3.65	5.0
2. Small σ_5		
$n_c = 10^{18} \text{ cm}^{-3}$ at $t_p/2$	2.06	3.9
$n_c = 10^{18} \text{ cm}^{-3}$ at t_p	1.98	3.8

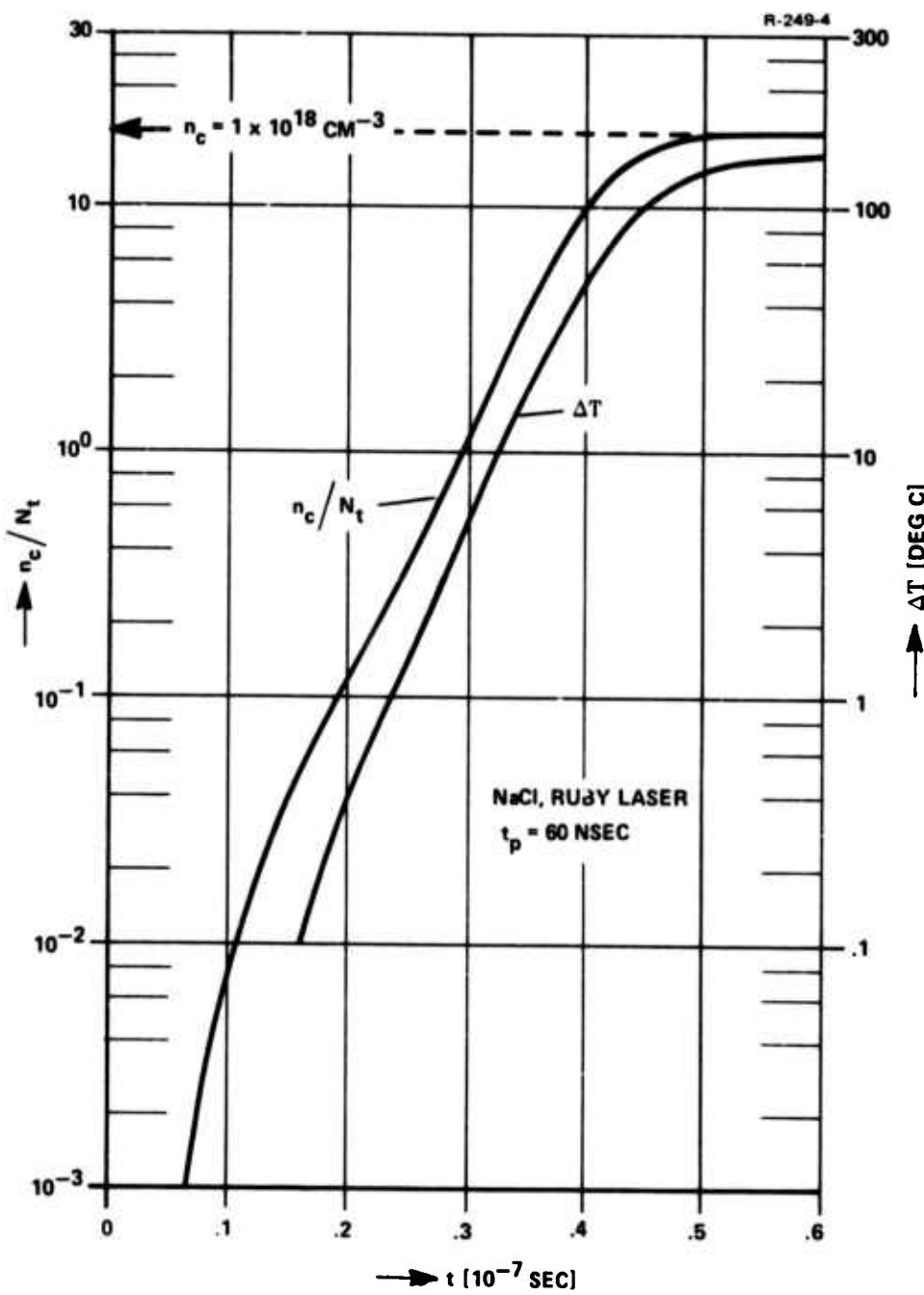


Figure 6 - The rise of the free electron concentration and of the temperature during the exposure of a NaCl crystal with a uniform 60 nsec pulse from a ruby laser having a peak flux of 1.865×10^{28} photons per cm^2 and sec.

Standard sample, avalanche ionization rate: from equation (14)

Five-photon cross section: $\sigma_5 = 0.5 \times 10^{-140} \text{ cm}^{10} \text{ sec}^4$.

the A^* is selected so that damage, defined by $n_c = 1 \times 10^{18} \text{ cm}^{-3}$, occurs at the end of the laser pulse. The computations again are presented for our standard sample (NaCl, containing $5 \times 10^{16} \text{ cm}^{-3} \text{ Cl}^-$ -vacancies, 10% of them converted to F-centers). Both, avalanche and five-photon carrier generation, are considered. Increasing the peak flux A^* shifts the curves of Figure 6 upward. They intersect the dashed horizontal line (definition of damage) at successively shorter times. The relation between the concentration - defined damage threshold, and the time of damage occurrence is shown in Figure 7. Several observations may be made from Figure 7:

- Damage may occur at any time during the laser pulse; higher peak fluxes damage earlier
- Even in the absence of any statistics, it would require a well controlled and highly reproducible laser pulse to produce damage in the last quarter of the pulse duration; e.g., if damage is produced for a given flux A^* at $t = 60 \text{ nsec}$, it requires only 0.011% more peak flux for damage to occur at 54 nsec, 0.5% more flux to observe it as 48 nsec, and 3.6% more at 42 nsec. Even with a relatively stable laser such as the one described by Bass and Barrett³⁹ (maximum pulse-to-pulse energy variation of 2 to 5%) it would indeed by a "lucky event" to observe the occurrence of damage in this time range.

4.2.7 Recombination of Free Carriers After Exposure of NaCl to Laser Pulse Trapping

In this section, we discuss the mechanism by which electrons, generated by photon absorption and avalanche ionization, are trapped in Cl^- -vacancies. By calculation of the density of F-centers as a function of laser photon flux, we can evaluate the spatial variation of the trap density on the surface that was exposed to an intense laser pulse having

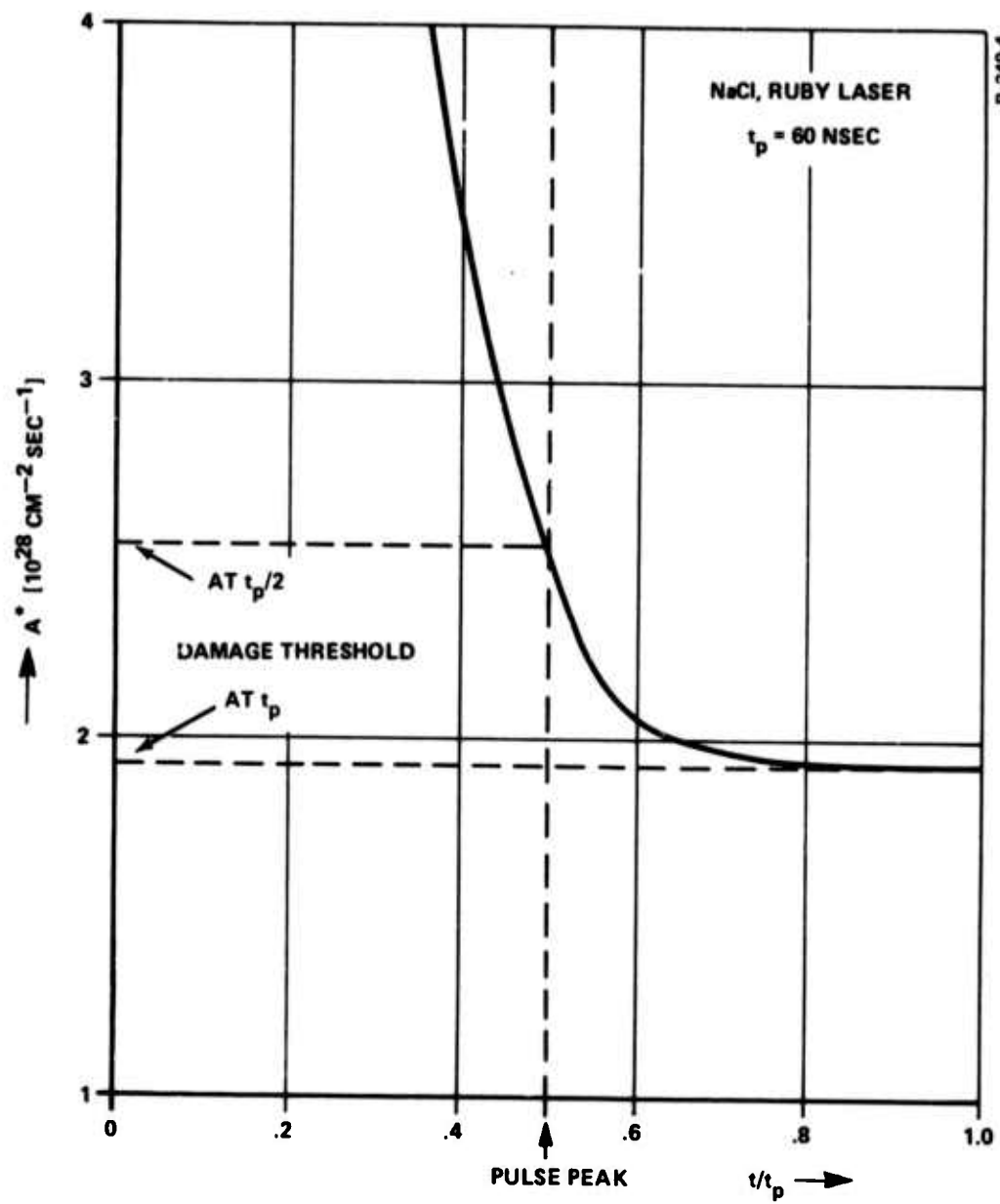


Figure 7 - Time of intrinsic damage occurrence as a function of the peak flux.

Laser: 60 nsec, ruby

NaCl: Same as in Figure 6

Damage Mechanism: Avalanche, aided by five-photon absorption
 $(\sigma_5 = 0.5 \times 10^{-140} \text{ cm}^{10} \text{ sec}^4)$.

a known photon flux profile. The effects of electron diffusion and temperature diffusion on the spatial distribution of the F-centers are described and the implications of the results vis-a-vis nondestructive laser surface damage testing are discussed.

The calculations are performed with the aid of the following rate equations, obtained from Eqs. (8)-(10) by dropping all terms containing photon induced transition rates:

$$\frac{dn_c}{dt} = n_t \omega_{tc} - n_c (N_t - X - n_t) \omega_{ct} - n_c / \tau_c \quad (18)$$

$$\frac{dn_t}{dt} = -n_t \omega_{tc} + n_c (N_t - X - n_t) \omega_{ct} - n_t / \tau_t \quad (19)$$

$$\frac{dX}{dt} = n_t / \tau_t \quad (20)$$

These equations are solved for $t \geq t_p$ using as initial concentrations the concentration $n_c(t_p)$, $n_t(t_p)$ and $X(t_p)$, and the temperature $T(t_p)$, obtained from Eqs. (8)-(11).

Figure 8 is a typical curve showing the concentration of F-centers as a function of the peak photon flux for a 60 nsec pulse at a time long after the end of the laser pulse ($t = 6\tau_c$). The NaCl crystal contains $5 \times 10^{16} \text{ cm}^{-3} \text{ Cl}^-$ -vacancies. The calculations were performed for 3 different initial F-center concentrations.

Pulses having a low peak flux ($A^* \leq 7 \times 10^{27} \text{ cm}^{-2} \text{ sec}^{-1}$) bleach the initial F-center concentration by two-photon absorption. At fluxes where multiphoton photocarrier generation and avalanche ionization are effective (compare Figures 2 and 3), the concentration of F-centers increases again. Finally, temperature bleaching sets in at fluxes close to the temperature-defined intrinsic damage threshold.

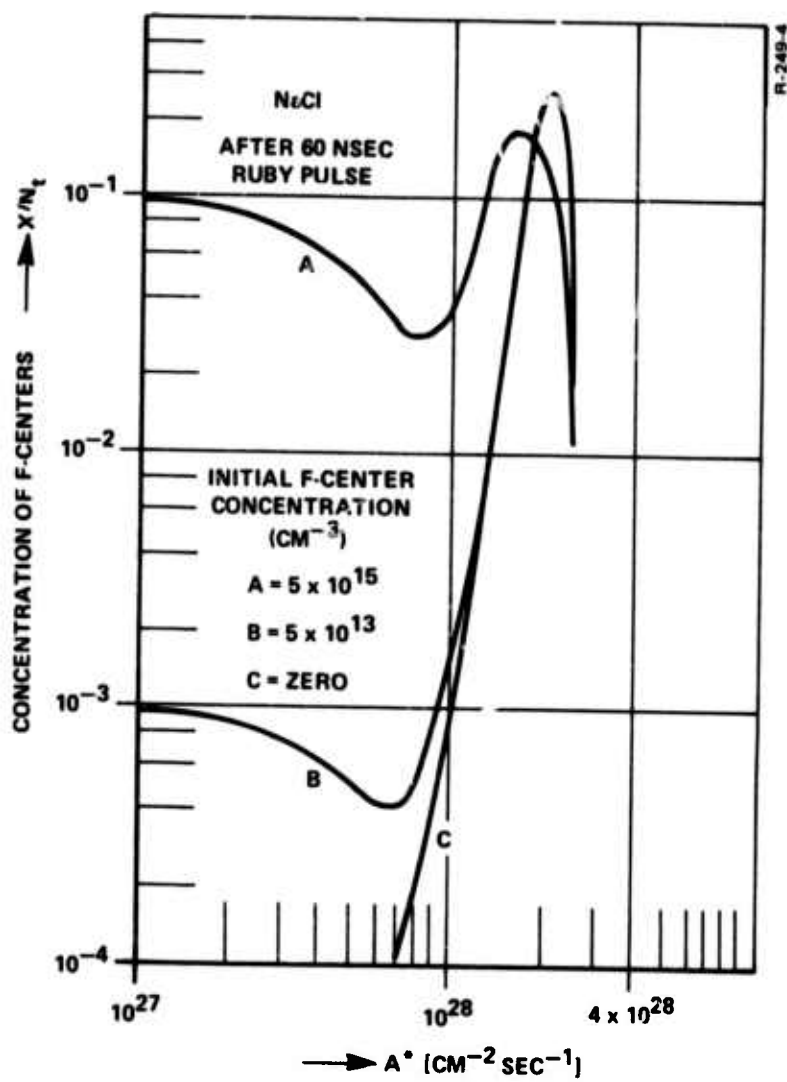


Figure 8 - Laser induced concentration of F-center in a NaCl crystal containing 5×10^{16} Cl^- -vacancies as a function of the ruby laser peak plus for various initial F-center densities. In this case, the damage thresholds are (in $10^{28} \text{ cm}^{-2} \text{ sec}^{-1}$):

- (a) Concentration-defined: 1.87
- (b) Temperature-defined: 2.1

Mechanism: Avalanche ionization and multiphoton absorption

$$\sigma_5 = 0.5 \times 10^{-140} \text{ cm}^{10} \text{ sec}^4$$

ω_1 from equation (14).

Similar curves are obtained after exposure of NaCl with shorter laser pulses. For this case, F-center concentrations close to the limit of complete filling of the Cl^- -vacancies are reached at peak fluxes slightly larger than the concentration-defined damage threshold.

In the case of a TEM_{00} laser pulse the concentration of F-centers $X(t > \tau_c) = f(A^*)$ is converted to the spatial variation of F-centers on the crystal surface via

$$A^* = A_0^* \exp(-r^2/d^2) \quad (21)$$

where A_0^* is the peak flux at $r = 0$, and d is the radius of the flux profile at which $A^* = A_0^*/e$. Typical trap and temperature distributions are shown in Figures 9 and 10.*

Results similar to those shown in Figures 8 and 9 are obtained in all other cases. For short pulse durations ($t_p \leq 10^{-9}$ sec), however, F-center bleaching cannot be observed at the concentration-defined damage threshold, because at that flux the sample temperature has not increased sufficiently. Complete bleaching always occurs, at the temperature-defined threshold flux and somewhat below. The presented calculations permit several conclusions:

- A characteristic ring-shaped spatial trap-distribution is obtained in NaCl that was exposed to a ruby laser pulse having a peak flux close to the intrinsic damage threshold.
- Observation of "intrinsic" laser-induced exoelectron emission** from NaCl is an indication that the peak flux was between 30% and 100% of the threshold flux.

* As shown later, effects of electron and temperature diffusion on the trap distribution can be neglected in a first approximation.

** We define "intrinsic" exoelectron emission as due to electron emission from traps in the surface layer and not due to physico-chemical reactions in the absorption layer.

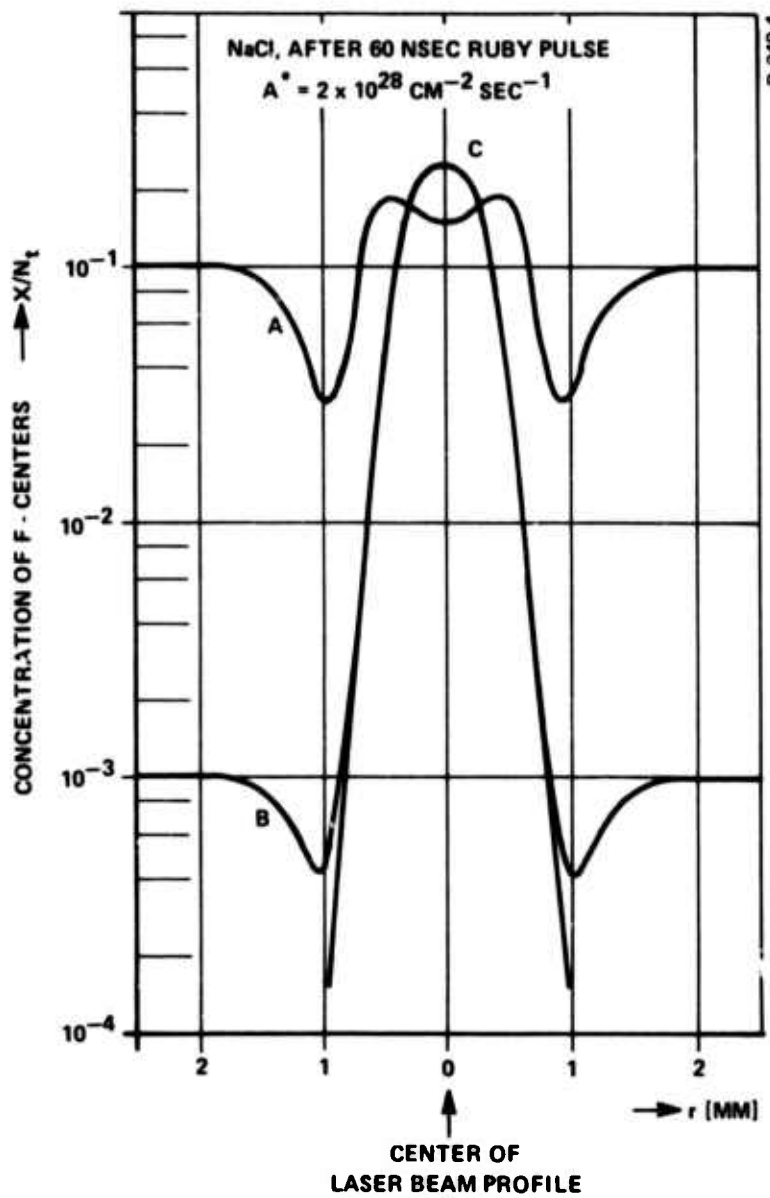


Figure 9 - Spatial distribution of F-centers along the surface of a NaCl crystal that was exposed to a 60 nsec ruby laser pulse having a peak flux of $A^* = 2 \times 10^{28}$ photons per cm^2 and sec. The curves correspond to the ones in Figure 8. The crystal contains $N_t = 5 \times 10^{16} \text{ cm}^{-3} \text{ Cl}^-$ -vacancies. Initial F-center densities are

- A. $0.5 \times 10^{15} \text{ cm}^{-3}$
- B. $5 \times 10^{13} \text{ cm}^{-3}$
- C. zero

$d = 1 \text{ mm}$

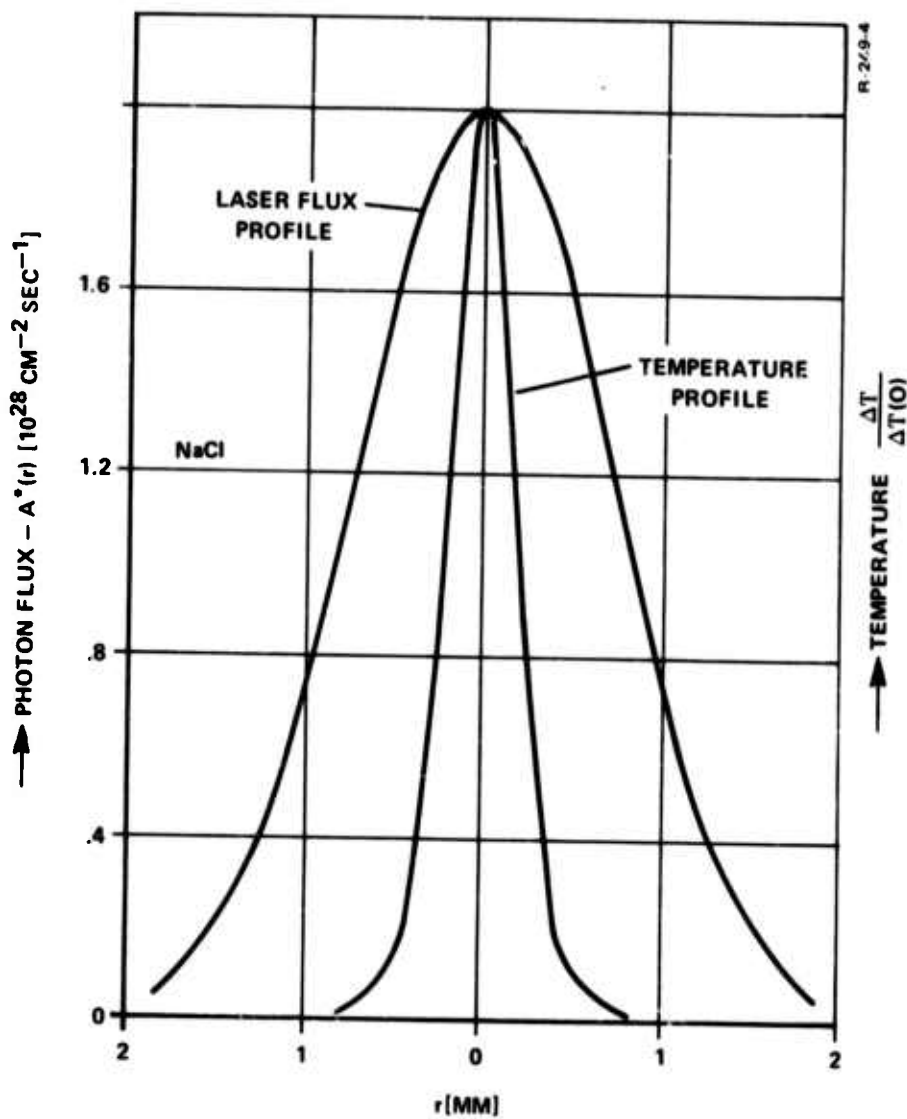


Figure 10 - Laser flux profile and normalized temperature profile of the standard NaCl crystal that was exposed at room temperature to a 60 nsec TEM_{00} mode ruby laser pulse having a peak flux $A^* = 2 \times 10^{28}$ photons per cm^2 and sec. The temperature increase ΔT at the center of the pulse was $390.4^\circ C$.

- The "shape" of the trap distribution (or the exoelectron image - see Section 4.2.8) indicates the proximity of the peak flux to the temperature-defined damage threshold. A center minimum occurs only at fluxes just below the temperature-defined threshold.

4.2.8 Diffusion Effects

Diffusion may effect the spatial trap distribution (Figure 9) in two ways. First, the distribution may be broadened by electron diffusion without a decrease of the total number of generated F-centers. Second, the center minimum created by a sharp rise in temperature at photon fluxes somewhat below the temperature-defined damage threshold may broaden by thermal diffusivity and thus increase the diameter of the bleached area around the laser axis.

Let us consider a NaCl-crystal of about 1 mm thickness as typically used in our experiments. In this case, a cylindrical laser beam waist is assumed. In a first approximation, the laser flux is constant along the axis for peak fluxes up to the damage threshold. Under these conditions, and neglecting surface heat loss the solution of the diffusion equation is⁴¹

$$\Delta T(r, t) = (2Dt)^{-1} \int_0^{\infty} \exp [-(r^2 + r'^2)/4Dt] f(r') I_0 \left(\frac{rr'}{2Dt} \right) dr' \quad (22)$$

where

I_0 = modified Bessel function

$f(r)$ = temperature profile at $t = 0$ (see Figure 10)

r = distance from the laser axis

$D = 0.0187 \text{ cm}^2 \text{ sec}^{-1}$ (thermal diffusivity coefficient of NaCl).

We computed $T(r)$ at various times after the end of the laser pulse. The results turned out to be similar to those obtained by an initial temperature distribution of the form

$$\begin{aligned}f(r) &= \Delta T(0,0) \text{ for } r < d/3 \\&= 0 \quad \text{for } r > d/3\end{aligned}$$

where d is the $1/e$ -radius of the laser flux profile. Solutions of this particular diffusion problem are given in Ref. 41.

On the axis, the temperature decreases with time according to

$$\Delta T(0,t) = \Delta T(0,0)[1 - \exp(-d^2/4Dt)] \quad (23)$$

At the beam center, the temperature decreases to half its peak value in the time $\tau = d^2/4D \ln 2$. The width of the temperature profile at $1/2 T(0,0)$ hardly changes during this time. In other words, no part of the crystal except for an axial cylinder of radius $d/3$ even experiences a temperature above $1/2 T(0,0)$. Only this cylindrical volume may be affected by thermal bleaching. The degree of bleaching is, of course, a function of the temperature dependent lifetime ω_{FC}^{-1} of the F-center and of τ . ~~urable~~ effects are expected only for $\omega_{FC}^{-1} \leq \tau$.

For a laser beam with $d = 1$ mm, τ is about 20 msec. The lifetime of the F-center, on the other hand, decreases to this value only at around $850-900^\circ\text{K}$. This means thermal bleaching continues after the laser pulse only when the peak laser flux is very close to the temperature-defined intrinsic damage threshold and it would effect only the axial volume in the immediate vicinity of the beam axis. This bleaching will deepen the minimum of the trap distribution slightly with practically no effect on the width.

Diffusion of the electron concentration $n_c(r,t)$ is described by an expression analogous to Eq. (22). The spatial trap distribution is affected only by diffusion processes that occur in a time

shorter than the free electron lifetime $\tau_c \approx 10^{-6}$ sec. We have calculated the influence of electron diffusion on the trap density $n_c(r, t > t_p)$ and found it to be negligible except for laser beams where $d \leq 10\mu$.

4.2.9 Laser Induced Exoelectron Emission

In Phase (3) (see Section 4.1), the laser induced concentration of F-centers is measured by monitoring the emission of exoelectrons.

We do not present a phenomenological theory of EE here, but rather refer to a paper by Kelly²³ who recently investigated the kinetics of TSEE. It suffices to say that laser induced exoelectron emission was found to be very weak in all materials investigated during this contract. Experimental results are summarized in Section 5.3.

4.3 APPLICATION TO NDT OF LASER SURFACE DAMAGE

In the previous sections we described the mechanism by which exoelectron emission is observed after exposure of a transparent dielectric material (in particular NaCl) to a laser pulse having a peak flux that is close to the temperature-defined intrinsic damage threshold. We have not distinguished between bulk damage and surface damage because the intrinsic damage process is physically identical in both cases.

Laser induced trap filling in NaCl occurs at photon fluxes that are a factor of 2 to 3 smaller than the damage threshold. In general, exoelectron emission resulting from these trapped electrons is very weak so that measurable effects are observed only when the flux approached the intrinsic damage threshold. These findings form the basis for the discussion of EE-techniques as potential NDT-methods for laser surface damage. Unfortunately, experimental work planned for the contract period has not progressed sufficiently to provide concrete data at this time.

NDT-testing has to detect two types of processes that may reduce the surface damage threshold:

- (1) Intrinsic damage enhanced by the presence of impurities and surface flaws (small pits, grooves, or scratches)
- (2) Damage caused by light absorbing inclusions

Impurities increase the cross-section for photocarrier generation and surface flaws result in local enhancement of the optical field strength.⁴² In both cases the photon flux required for the generation of filled traps as well as for damage is reduced. In a sample that contains a high concentration of impurities or which is scratched exoelectron emission may be observed after exposure to laser fluxes below the intrinsic damage threshold. In this case, EE techniques may be useful as NDT-methods. However, as discussed in the next section, feasibility has yet to be demonstrated.

Inclusions absorb light and locally increase the temperature. Large inclusions generally cause damage at photon fluxes far below the intrinsic value; therefore EE-techniques are inherently unsuited as NDT-methods for large inclusions. Small absorbing inclusions (radius $\leq 0.01\mu$) may not cause optical damage at longer pulse lengths (e.g., Q-switched laser pulses), but may reduce the damage threshold at subnanosecond laser pulses.¹¹ Conceivably then, the effect of the heat absorbed by small inclusions at fluxes close to the intrinsic threshold may locally alter the trap distribution. The question is whether or not this causes any observable changes in the exoelectron emission current. Certainly, the surface area affected would have to be sufficiently large to be resolved by the exoelectron imaging device. Considering the limitations of the exoelectron microscope (EE intensity, magnification, etc.) described in Section 5.1, this appears questionable at this time. However, an answer may only be found by further experimental work.

SECTION 5

EXPERIMENTAL FACILITIES FOR MEASUREMENT OF GENERAL EXOELECTRON EMISSION PROPERTIES OF LASER MATERIALS

The idea of using laser-induced exoelectron emission as an NDT method was based on our original experiments with LiF.² Ring-shaped TSEE images were obtained at the entrance surface of a cleaved and polished Harshaw crystal after exposure to a single 50-nsec pulse from a Q-switched Nd-glass laser. Images of this type were produced at peak laser flux levels above, as well as somewhat below, the surface damage threshold; in one particular case, TSEE was also observed from the exit surface of the crystal. The inner diameter of the ring-shaped TSEE image was found to correspond approximately to the minimum spot size of the laser beam and always coincided with the location of the damage site, when damage occurred. Until these experiments were repeated under more controlled conditions, we had worked under the assumption that the observed TSEE images originally seen were the result of a direct interaction between the laser beam and the LiF crystal. We have since demonstrated, rather convincingly, that this assumption is not correct. Instead, it is now clear that, at relatively low peak levels, the presence of a spark associated with air breakdown at or immediately in front of the sample surface is needed to induce TSEE from this surface. In the absence of a spark, no emission is detectable, whether the entrance surface is damaged or not.

This discovery, for which we now have a tentative explanation, has forced a major revision of the originally anticipated experimental approach. At the beginning of this project we thought that the study of general EE properties of a number of selected optical materials would lead to a straightforward investigation of the laser induced EE effects and their interpretation. These investigations proved to be far more

difficult than anticipated. Some materials, such as glass and ruby, exhibited extremely low exoelectron emission, while others, such as pyroelectric LiNbO_3 , emitted without previous trap filling by ionized radiation. Most materials exhibited damage before any emission was observed. A major problem was the irreproducible character of the laser output. Fluctuations up to a factor of three in the shot-to-shot photon flux, originally considered tolerable, rendered much of the data useless because, as the theory of laser-induced EE laser showed, emission is measurable only for power levels immediately below the intrinsic damage threshold. The laser output fluctuation prevented study of this critical range of the laser power. Although the experimental situation was corrected recently, we were unable to obtain pertinent experimental information in the present contract period.

Before discussing the results of our experiments and their implications, we shall describe the experimental facilities. Two separate test systems were built. Both were designed for the investigation of the exoelectron emission characteristics of a broad range of laser and nonlinear optical materials under well-defined, reproducible conditions. One of these systems - the laser test facility - is equipped with an exoelectron emission microscope⁴ which provides the necessary imaging capability for a detailed study of laser-induced EE.

5.1 EXOELECTRON EMISSION TEST FACILITIES

A schematic diagram of the test apparatus is given in Figure 11. The basic components of this system include: (1) an adjustable electron gun, (2) an electrically-heated sample holder (for TSEE), (3) a photo-stimulation system (for OSEE), and (4) a Channeltron electron multiplier. These items are mounted inside a glass bell jar and the system is maintained under vacuum ($< 5 \times 10^{-7}$ Torr) with a well-trapped oil diffusion pump. Provisions for introducing controlled partial pressures of high-purity gases into the system are also available.

The electron gun, which is used as a source of ionizing radiation (for trap filling), is a pentode having two-dimensional deflection capability. The beam diameter, beam intensity, and beam energy are all

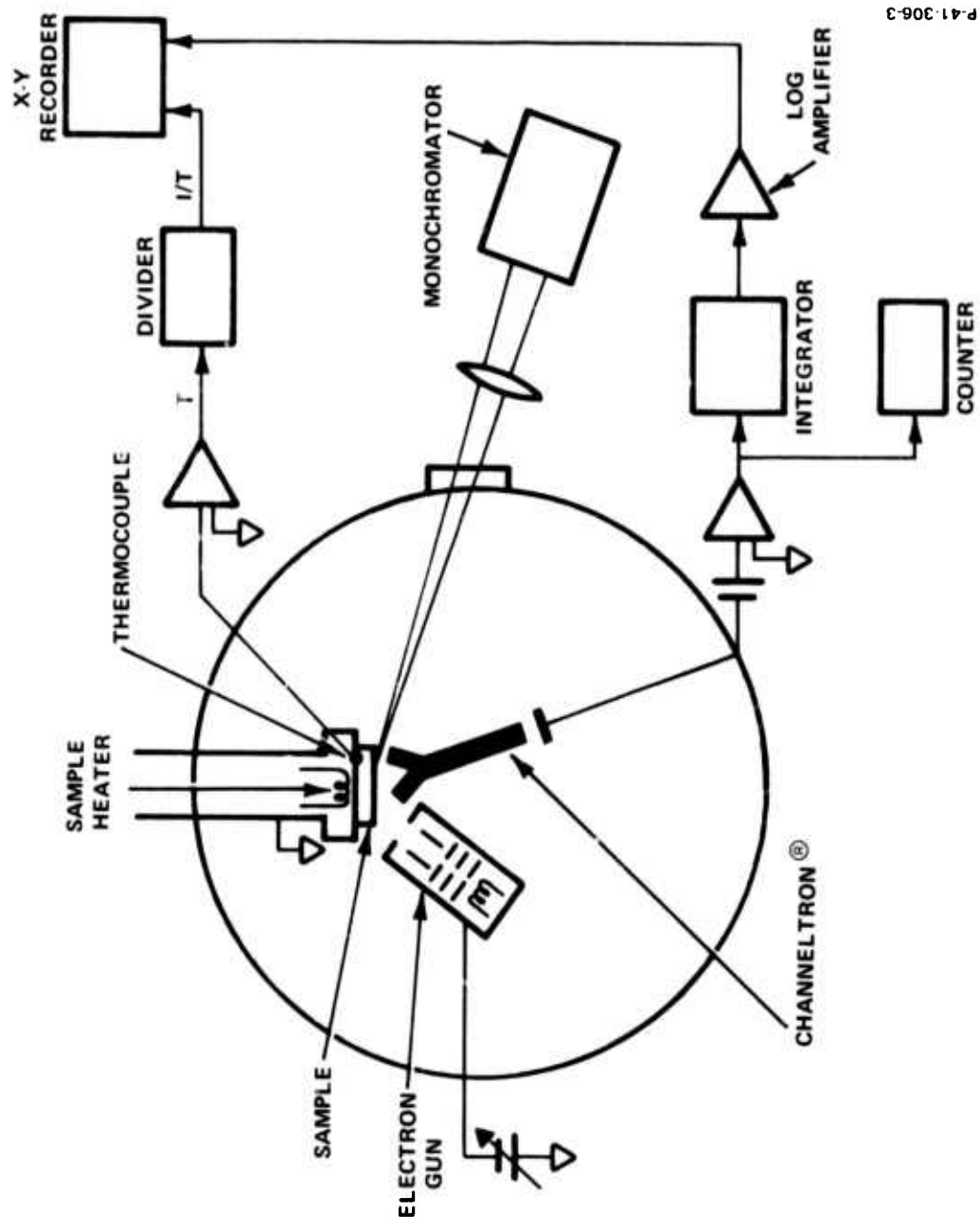


Figure 11 - Schematic diagram of the general exoelectron emission test system.

adjustable so that the total flux of electrons incident on a given specimen area can be controlled and reproduced. The copper sample holder to which the specimens are attached can be heated at programmed rates and can also be cooled to liquid nitrogen temperatures. A thermocouple inserted in a small hole in the copper block is used to monitor the specimen temperature. Appropriate shielding is employed so that any signal resulting from thermionic emission from the metal specimen holder itself will be minimized. The optical stimulation system consists of a high-intensity UV light source and monochromator together with auxiliary lenses and slits for focusing and collimation; a quartz window into the vacuum system is also provided.

The Channeltron electron multiplier and associated detection electronics operate over a wide dynamic range, thus allowing the collection of data on a broad variety of materials ranging from very weak EE emitters such as glass to strong emitters such as BeO. In situations where the emission rate is low, the electron multiplier can be operated in a pulse counting mode, the output pulses being counted and stored in a 400-channel analyzer. In normal situations, the output of the Channeltron is fed to an integrator circuit and the resulting signal is amplified and displayed. Exoelectron proximity images could be obtained with this facility with the aid of a microchannel bundle or, if very high gain was required, with a Chevron multiplier bundle⁴³ (Figure 12).

The laser-induced EE and surface damage test facility, schematically shown in Figure 13, allows a sample to be exposed to well-characterized laser pulses while being maintained under high vacuum. The system consists essentially of: (1) an oil-diffusion-pumped specimen chamber which houses an electrically heated sample holder-manipulator; (2) a Korad K-1 Nd-glass or ruby laser mounted on an optical table; (3) equipment for measuring the absolute energy of the laser beam, and for monitoring the waveform of the laser pulse as well as the spatial flux distribution within the focused beam; and (4) an auxiliary He-Ne laser used to obtain precise alignment of the experimental laser relative to the specimen surface.

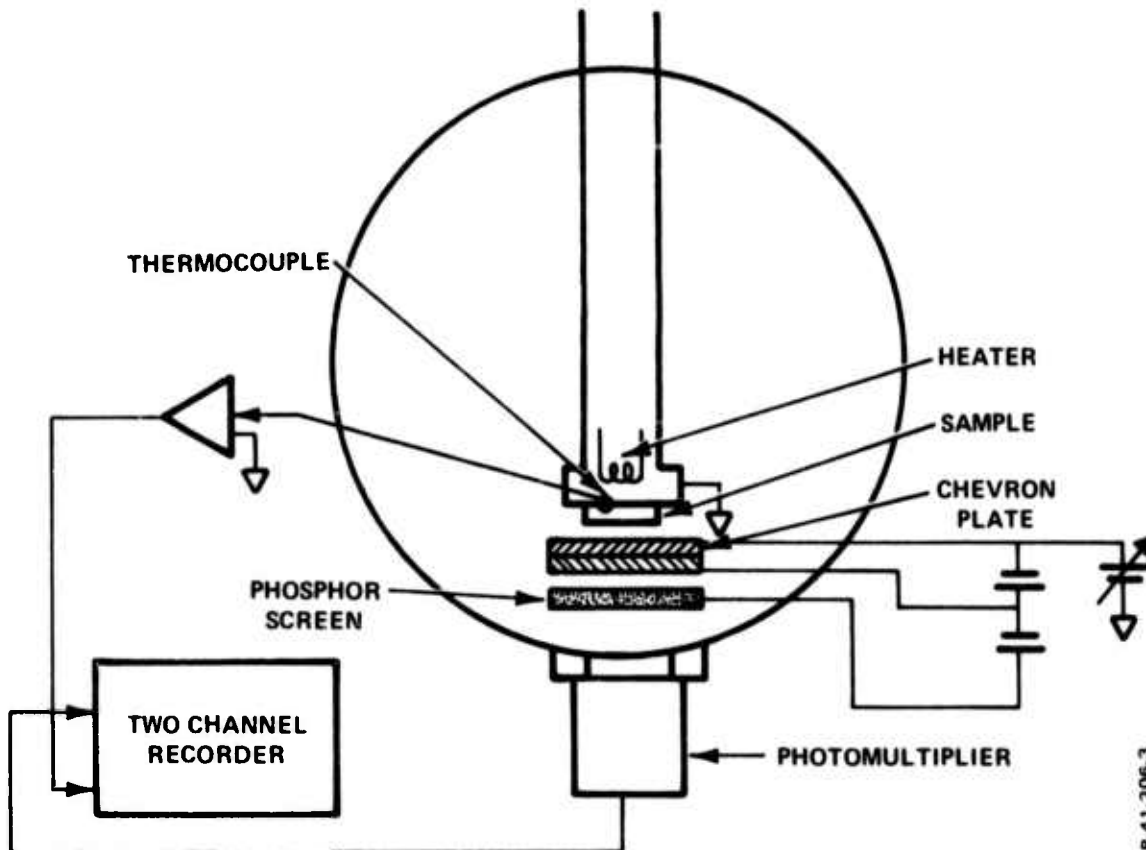


Figure 12 - Exoelectron imaging system.

When mounted in good thermal contact with the specimen holder, the surface of the sample under examination faces an optical window in the vacuum chamber through which the laser beam enters. The sample holder, in turn, is attached to a manipulator providing linear translations (X and Y) in a plane normal to the axis of the incident beam as well as rotation about a vertical axis normal to the beam. Thus, the specimen can be positioned so that any selected region of the surface can be exposed to the laser beam. Accurate alignment of the specimen surface normal to the incident laser beam is accomplished with the manipulator and the auxiliary laser.

The construction and principle of operation of this microscope is simple.⁴ It consists of a single electrostatic lens (immersion lens)

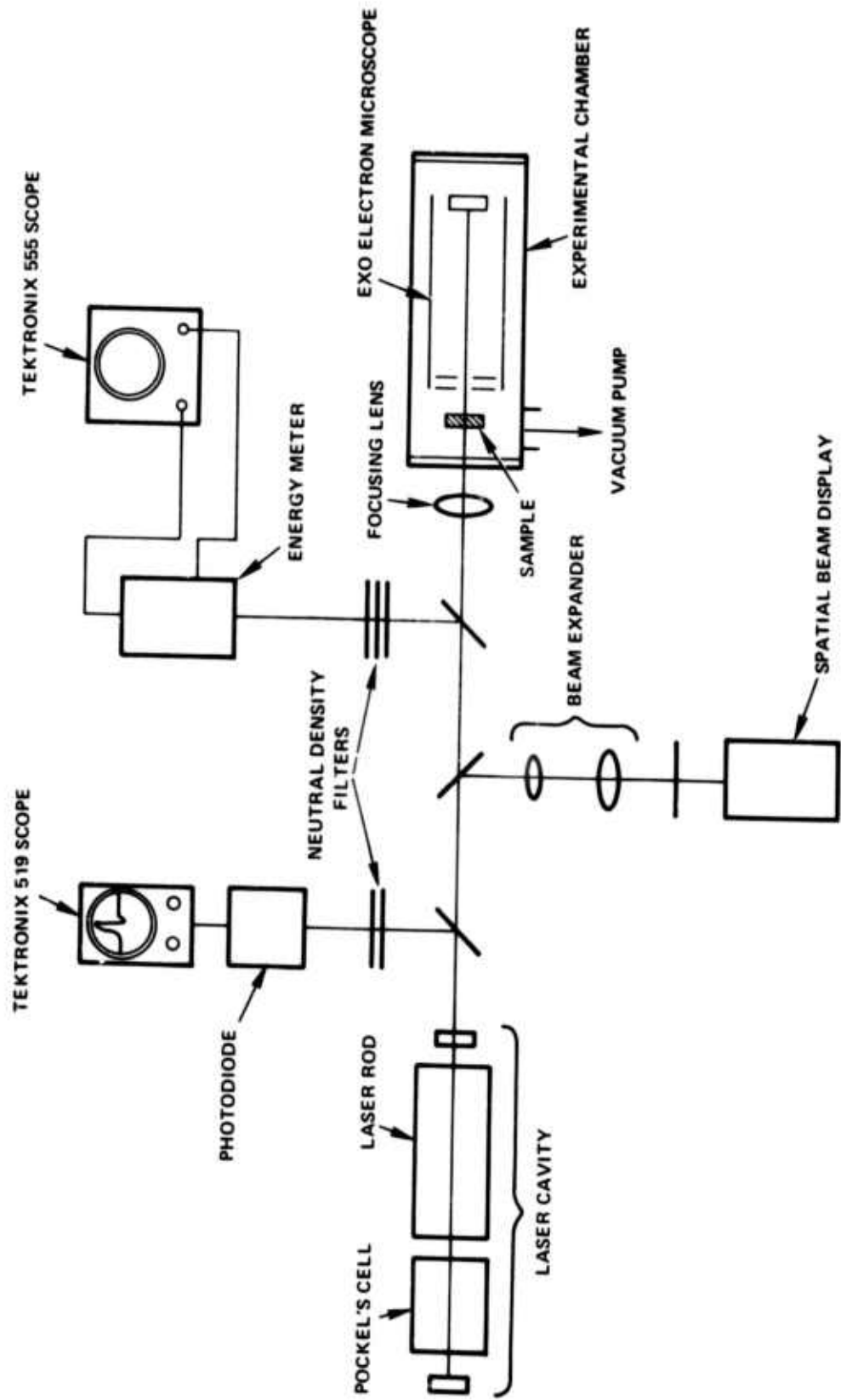


Figure 13 - Schematic diagram of the laser-induced exoelectron emission and surface damage facility.

which focuses exoelectrons emitted from the specimen surface onto a micro-channel plate electron multiplier located immediately in front of a phosphor screen. The magnification is limited to about 100X. Because of the experimental problems associated with laser-induced EE, we have postponed the microscope work and concentrated on measurements of thermally or optically stimulated EE using the special sample holder shown in Figure 14.

The Korad K-1 laser can be operated with either a Nd-glass rod or a ruby rod to give Q-switched pulses with a peak power output in excess of 100 MW (multi-mode). Tuning the plane-mirror cavity to achieve single (transverse) mode operation reduces the peak power output to about 5 MW. Strong external focusing is therefore needed to achieve the required peak intensity in the single TEM_{00} transverse mode.

A fast-response photodiode (ITT 4000, rise time 0.65 nsec) and oscilloscope (Tektronix 519) are used to determine the energy and waveform of the Q-switched pulse. For absolute energy or intensity measurements of the laser pulse, the photodiode is calibrated against a bolometer. The spatial flux distribution of the beam is measured using a technique developed by Avizonis, Doss and Heimlich.⁴⁴ The beam is divided by a beam-splitter and focused by identical lenses onto the specimen surface and the focal plane of a projector lens. The enlarged image of the focal neck of the beam, which is produced by the projector lens is recorded photographically and analyzed.

5.2 EXPERIMENTS WITH LiF

Initial experiments were carried out on a LiF crystal of uncertain quality using the Korad Nd-glass laser at Bendix. The damage threshold for this crystal was found to be about 15 J/cm^2 in a 50-nsec pulse (multi-mode). In multi-mode operation, Q-switched pulses of sufficiently high peak intensity could be obtained over a laser spot size of 1-2 mm diameter to observe TSEE by direct or proximity imaging.² Operating the Korad laser to give Q-switched pulses in the single TEM_{00} mode would have required that the laser spot size be reduced to below 100 μm to achieve sufficiently intense pulses. Direct imaging would therefore

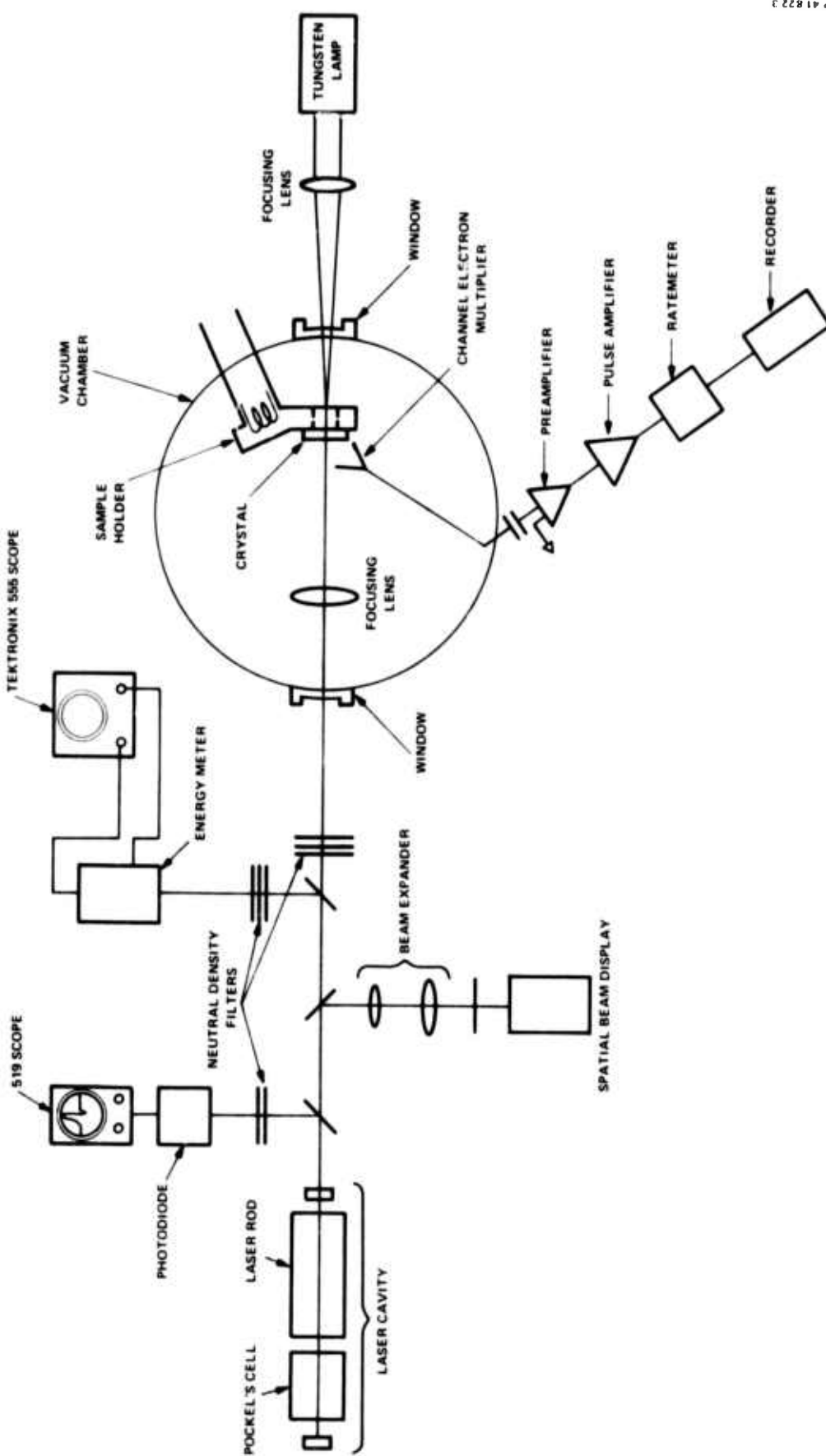


Figure 14 - Schematic diagram of apparatus used in studies of OSEE from laser-irradiated samples.

not have been feasible. To avoid this difficulty, arrangements were made to use the high-power single TEM₀₀ mode Nd-glass laser at the Owens-Illinois Research Center in Toledo, Ohio. It was our intention to duplicate the original experiments under more carefully controlled conditions. For this purpose several LiF crystals (1 x 1 x 1/16 in.) of optical quality were obtained from Harshaw Chemical Company.

With the Owens-Illionis Nd-glass laser, the damage threshold for these crystals was determined to be 20 J/cm² in a 30 nsec pulse. One of these crystals was exposed (in air) to a series of pulses of varying intensity, with each pulse directed at a different point on the specimen surface. Care was taken to space each successively exposed site far enough away from previously exposed areas to avoid laser bleaching. The peak laser photon flux during these individual pulses was varied from a value as low as about 1/6 of the damage threshold to a value well above the threshold damage level of 20 J/cm². In each case, the presence or absence of a spark associated with the laser pulse was monitored with a photographic camera. The crystal was then immediately transported to Bendix, and thermally-stimulated EE from the entrance surface of the crystal was searched for by direct imaging. Much to our surprise, no ring-shaped TSEE images such as we had seen in our original experiments were observed. In fact, no exoelectron emission was detected from any of the exposed sites at the entrance surface under conditions where a spark was absent during the laser pulse. This was true regardless of the peak intensity of the pulse, i.e., regardless of whether the surface was damaged or not. Thus, from these experiments we concluded that during exposure of the crystal to a relatively low peak intensity laser pulse, the occurrence of an air breakdown spark in front of the crystal surface was essential to the development of a TSEE image.

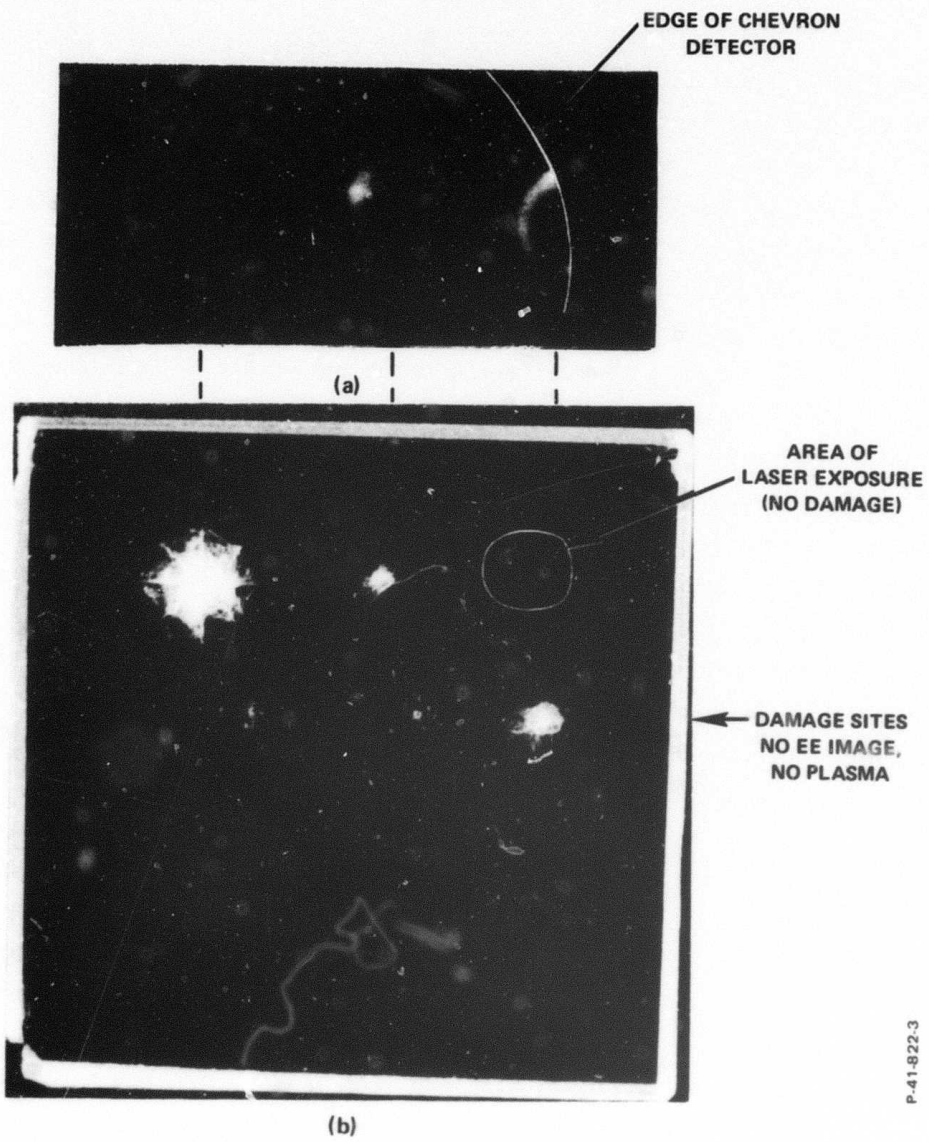
To verify this conclusion, the experiments were repeated on a similar LiF crystal using the multi-mode Nd-glass laser at Bendix. As before, a series of individual exposures were made at different peak pulse intensities; in addition, the position of the crystal relative to the focusing lens ($f = 14$ cm) was varied so that air breakdown could occur

in front of the entrance surface in some cases but not in others. The results, illustrated in Figure 15, confirm the conclusion that an air-breakdown spark is required to induce TSEE from LiF at relatively low ($<10^{28}$ photons - cm^{-2} - sec^{-1}) peak pulse intensities. Figure 15(a) is a low-magnification photograph of the LiF crystal showing the nature and extent of the damage produced as a result of various individual laser pulses while Figure 15(b) shows the corresponding EE images obtained from the entrance surface of the crystal upon subsequent thermal stimulation.

For the upper row of exposures in Figure 15(a), the crystal was positioned relative to the focusing lens so that an air breakdown spark occurred at or close to the entrance surface; ring-shaped TSEE images were obtained in each case. For the lower row of exposures, on the other hand, the crystal was moved closer to the focusing lens so that air breakdown did not occur at the entrance surface; none of these sites exhibited any thermally stimulated exoelectron emission.

The conditions under which the upper row of exposures in Figure 15(a) were made are worth describing in more detail. The upper left damage site was produced at a peak power level somewhat above the damage threshold (i.e., $>15-20 \text{ J/cm}^2$) with the laser beam focused roughly midway between the entrance and exit surfaces of the crystal. The center damage site in the upper row was obtained with the crystal in the same position relative to the focusing lens but with the peak pulse intensity reduced to a value just above the threshold for air breakdown; in this case, a spark occurred right at the entrance surface. The laser exposure at the upper right yielded a ring-shaped TSEE image without any visible surface damage. This was accomplished by moving the crystal about 1 cm farther away from the focusing lens while keeping the peak pulse intensity at or slightly above the air breakdown threshold; air breakdown occurred a few mm in front of the entrance surface. Apparently these were the conditions under which ring-shaped TSEE images without visible damage were first observed in LiF.²

A more convincing demonstration that TSEE images can be produced by an air-breakdown mechanism without direct interaction between the



P-41-822-3

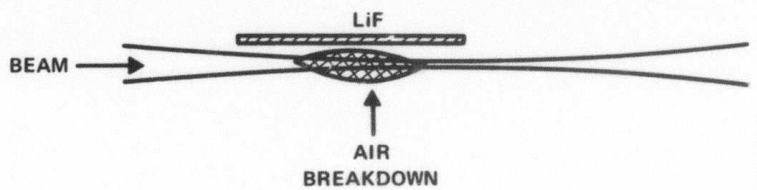
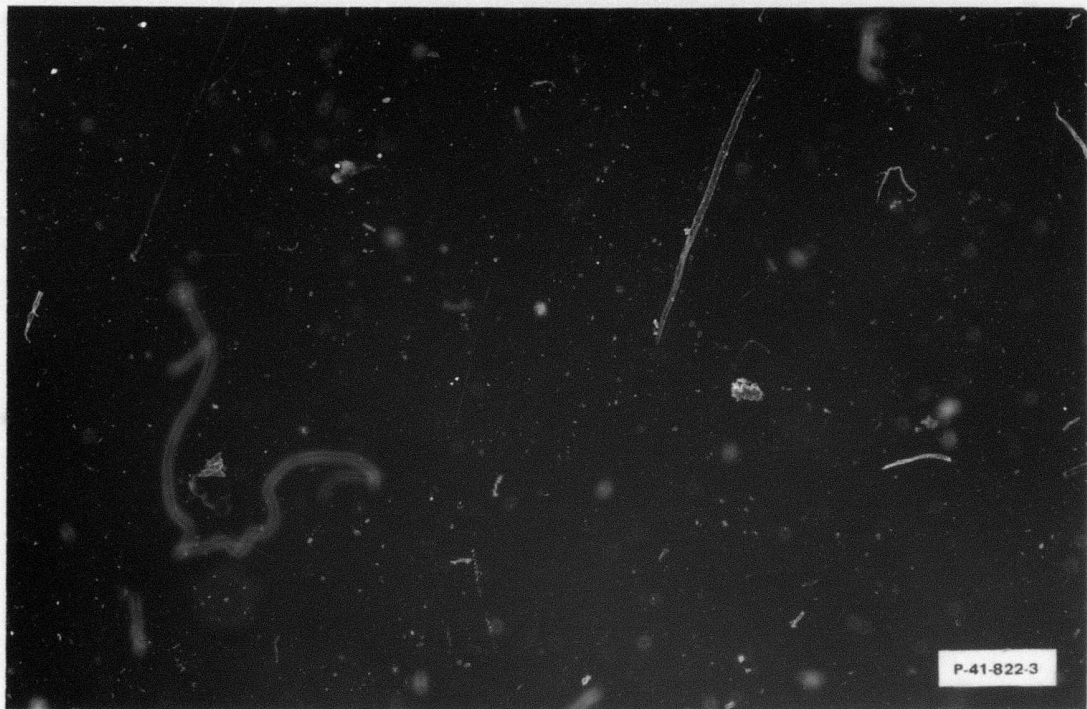
Figure 15 - Surface damage (a) and corresponding TSEE images (b) obtained from LiF after exposure to Q-switched 30-nsec pulses (multi-mode) from a Nd-glass laser.

For the upper row of damage sites in (a), air breakdown occurred in front of the entrance surface and TSEE was observed. During the laser exposures shown in the lower row, no air breakdown plasma was formed and no TSEE was observed. Magnification: 4X.

laser photon field and crystal is shown in Figure 16. A LiF crystal was oriented so that the focused laser beam passed parallel to the surface but a few mm away. When air breakdown took place in front of the crystal surface, a "cigar-shaped" TSEE image was observed (Figure 16(a)). In the absence of a spark adjacent to the crystal surface during the laser pulse, no exoelectron emission was detected.

With our present knowledge of the intrinsic laser damage mechanism in alkali halides, the results described above cannot be explained as being due to avalanche ionization of the sample materials. It is easy to estimate the rms field strength required for avalanche damage. From the ratio of the dc breakdown strength $E_{\text{LiF}} / E_{\text{NaCl}} = 2.7$, measured by Vorobev, et al.³⁶ and the rms optical breakdown strength $E_{\text{NaCl}} \approx 2.1 \text{ MV/cm}$, measured by Fradin, we obtain $E_{\text{LiF}} \approx 6 \text{ MV/cm}$ for Nd-photons which corresponds to nearly 400 J/cm^2 in a 30-nsec pulse. This value is far greater than the observed surface damage threshold of 20 J/cm^2 . Since the mechanism for intrinsic surface damage is basically the same as for bulk damage, this low threshold can only be explained by a rather poor surface finish of Harshaw's optical grade LiF crystals. Of importance are the implications of these findings in regard to the use of EE imaging as a NDT method for laser surface damage. We expect on the basis of the theory presented in Section 4, that only at sufficiently large peak fluxes A^* close to the onset of avalanche ionization, is a sufficient concentration of free carriers generated to produce the type of EE images that we had linked to the intrinsic damage mechanism. Poor surface finish and, particularly, inclusions lead to damage before these conditions are fulfilled.

EE imaging experiments with a laser-grade LiF, supplied by Harshaw, are in progress at the time this report was prepared. The work continues under sponsorship provided by the National Science Foundation. The question of EE image formation by the interaction of the plasma with the LiF surface remains to be answered as well. Recent measurements on laser-produced plasmas in 30 Torr of helium by Johnson and Chu⁴⁵ show the development and evolution of radial electron density profiles with on-axis minima. It appears possible that the formation of ring-like EE images



P-41-822-3

Figure 16 - Exoelectron images of a LiF single crystal that was placed parallel to the axis of the laser beam waist so that the air breakdown spark occurred in front of the crystal as shown schematically.

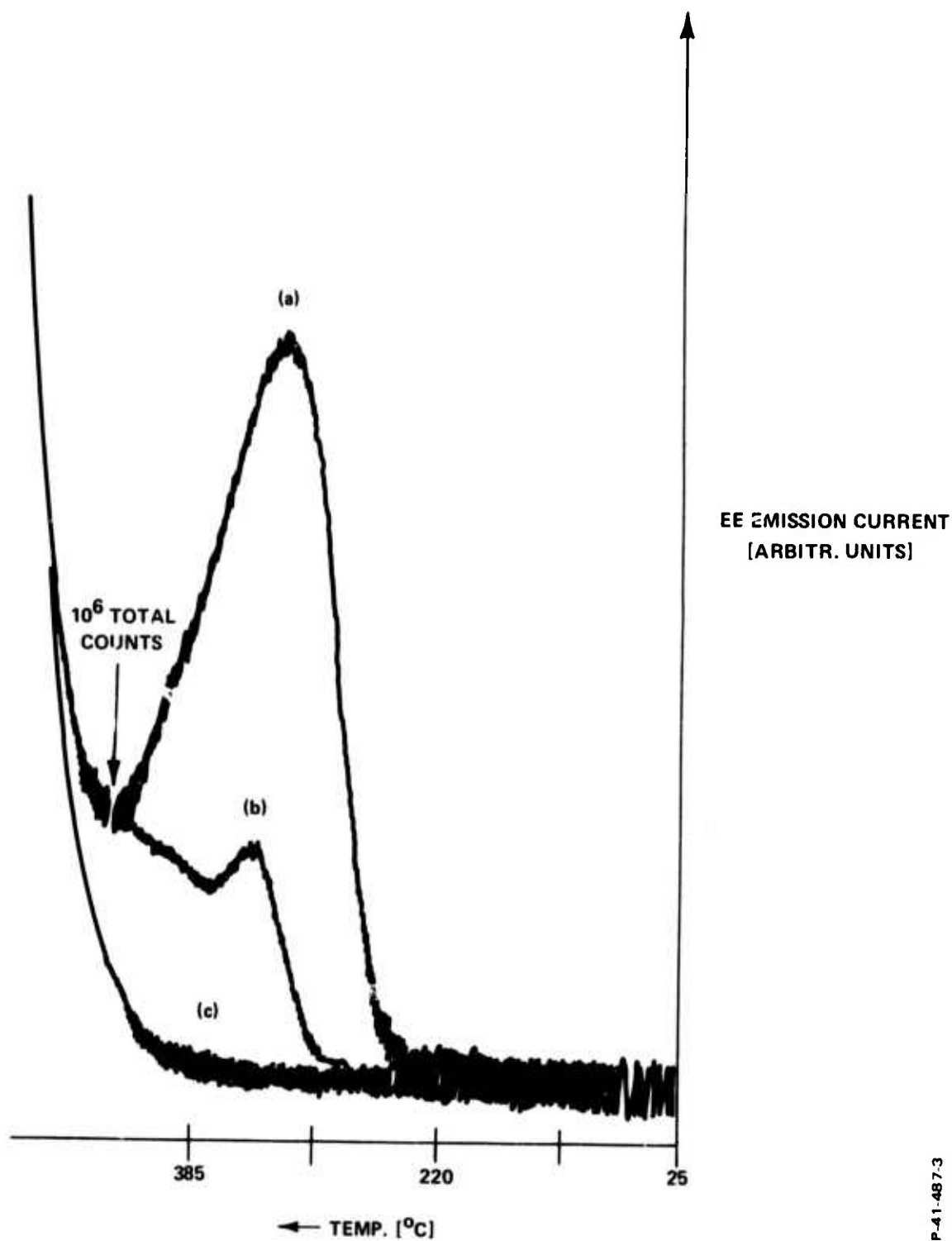
is caused by trapping of electrons from the plasma that propagates toward the crystal surface.

5.3 SUMMARY OF EE-EXPERIMENTS ON LASER GLASS, SODIUM CHLORIDE, AND LITHIUM NIOBATE

Little was known about exoelectron properties of laser materials at the start of this contract. Therefore, after the establishment of the facilities described in Section 5.1, we measured exoelectron emission from a number of materials after electron bombardment and laser exposure. The test apparatus proved to be very sensitive. We reproduced TSEE curves from nominally pure NaCl and measured for the first time thermally stimulated exoelectron emission from ED 2-glass after electron bombardment (Figure 17). The emission turned out to be rather weak. In a series of tests that included exposure of the glass samples to the Nd-glass laser at the Owens-Illinois Research Laboratories, we were unable to find conclusive evidence for exoelectron emission at laser powers below, at, and above the surface damage threshold. Exposure to ruby laser light yielded similarly negative results.

We then studied EE properties of nominally pure poled single crystalline LiNbO_3 . A new effect was discovered, namely, thermally stimulated field emission of electrons.²² This effect was described in the First Semiannual Report (AFCRL-TR-0068). As a result, optical stimulation techniques had to be used to study exoelectron emission from LiNbO_3 . We found a number of unexplained new OSEE phenomena after electron bombardment of the material. After laser exposure, measurable OSEE could be detected only at or above the laser surface damage threshold (for details see AFCRL-Report TR-73-0591).

In conclusion, the exoelectron properties of LiNbO_3 were found to be complex and, especially with regard to thermally induced field emission, rather interesting. However, just as in the case of laser glass, there is little hope to use these properties as a NDT method for laser surface damage. For this reason OSEE from LiNbO_3 was not investigated further.



P-41-487-3

Figure 17 - TSEE from ED-2 glass after electron bombardment (3 keV, 6×10^{-7} A/cm²) for: (a) 10 min, (b) 150 sec, and (c) 0 sec.

Experiments carried out with laser quality NaCl crystals from Harshaw have resulted in the first evidence that laser exposure can indeed fill traps by the mechanism described in Section 4. Subsequent heating of the sample between 230 and 300°C leads to exoelectron emission.

We first confirmed the existence of F-center peaks in our samples by measuring TSEE curves from electron-bombarded NaCl samples. A typical result is shown in Figure 18. The pronounced double peak corresponds to the peaks identified as the F-peaks by Bohun.¹³ An analysis by Sladsky,⁴⁶ who applied a relation developed by Braunlich,⁴⁷ yielded an activation energy of $E_F = 2.3$ eV, in reasonable agreement with values stated by Markham.³³

Laser-induced TSEE peaks are considerably weaker than those obtained after electron bombardment. The EE apparatus has to be used in its most sensitive mode. With high sensitivity, a rather pronounced emission from unexposed NaCl samples was measured at temperatures below the F-peak (Figure 19). Only after heating the sample to above 300°C can this emission be eliminated. Thereafter, the sample is useful for laser experiments. However, trap filling occurs only at laser fluxes that are within about 30 to 50% of the damage threshold. With the poor shot-to-shot reproducibility of our Korad laser, it was virtually impossible to approach these flux levels in a controlled manner. Below these levels no TSEE is expected, whereas above, the sample is destroyed since due to the breakdown, plasma material is deposited on the sample surface. The surface then has to be repolished before further experimentation. Laser induced TSEE was therefore measured only for "lucky" shots. A typical example, obtained with a multi-mode ruby laser pulse is shown in Figure 20.

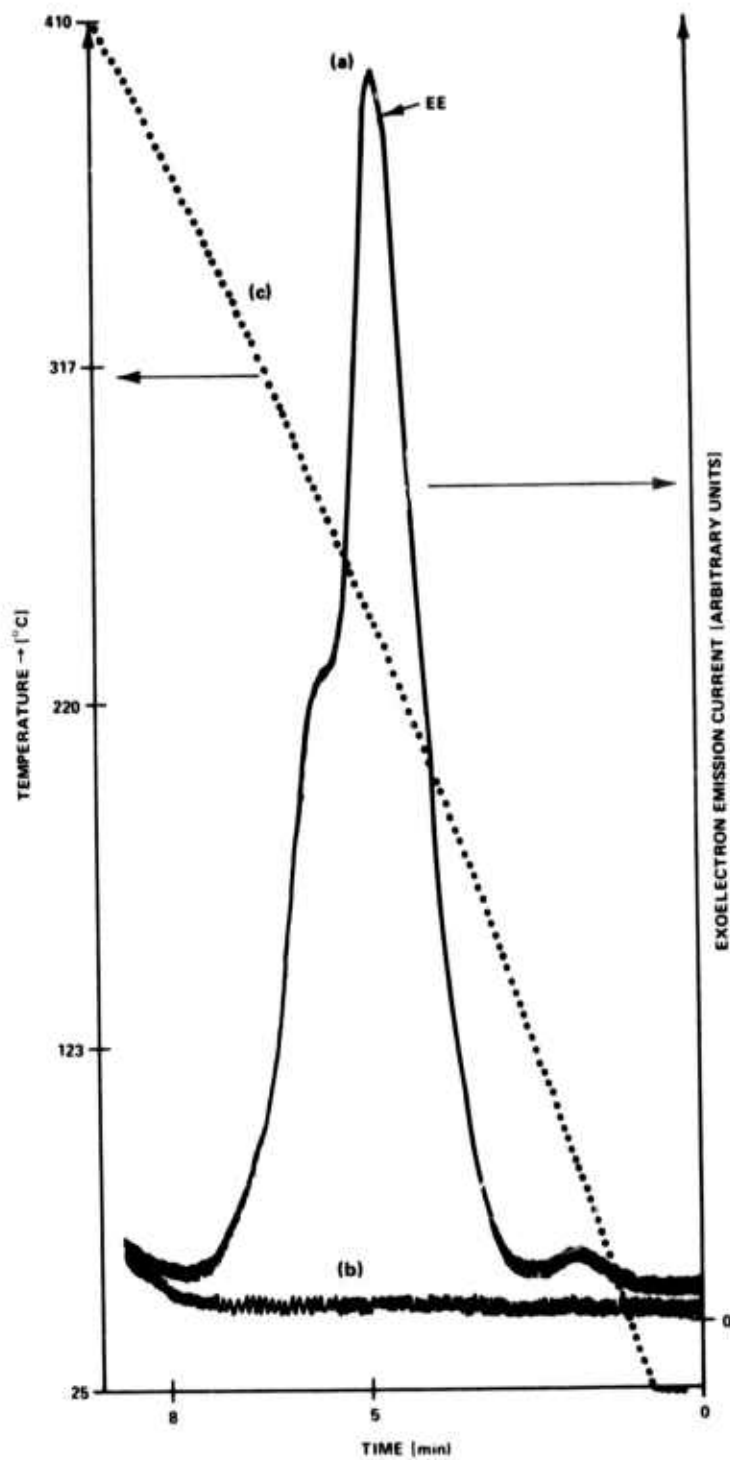


Figure 18 - TSEE for NaCl: (a) exoelectron emission after electron excitation, (b) emission with no prior electron excitation, and (c) temperature profile.

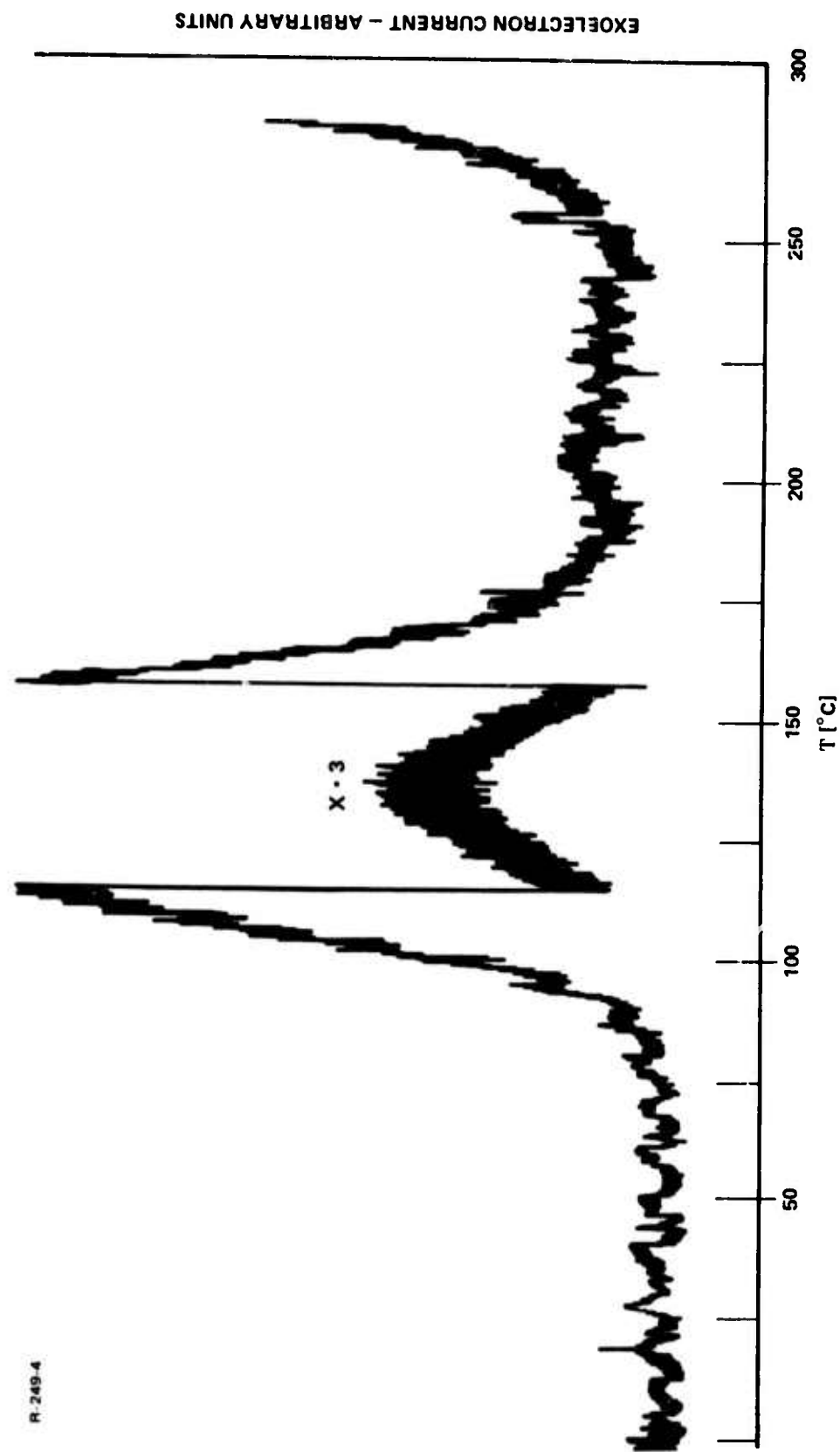


Figure 19 - Negative charge emission from a fresh NaCl crystal without laser exposure.

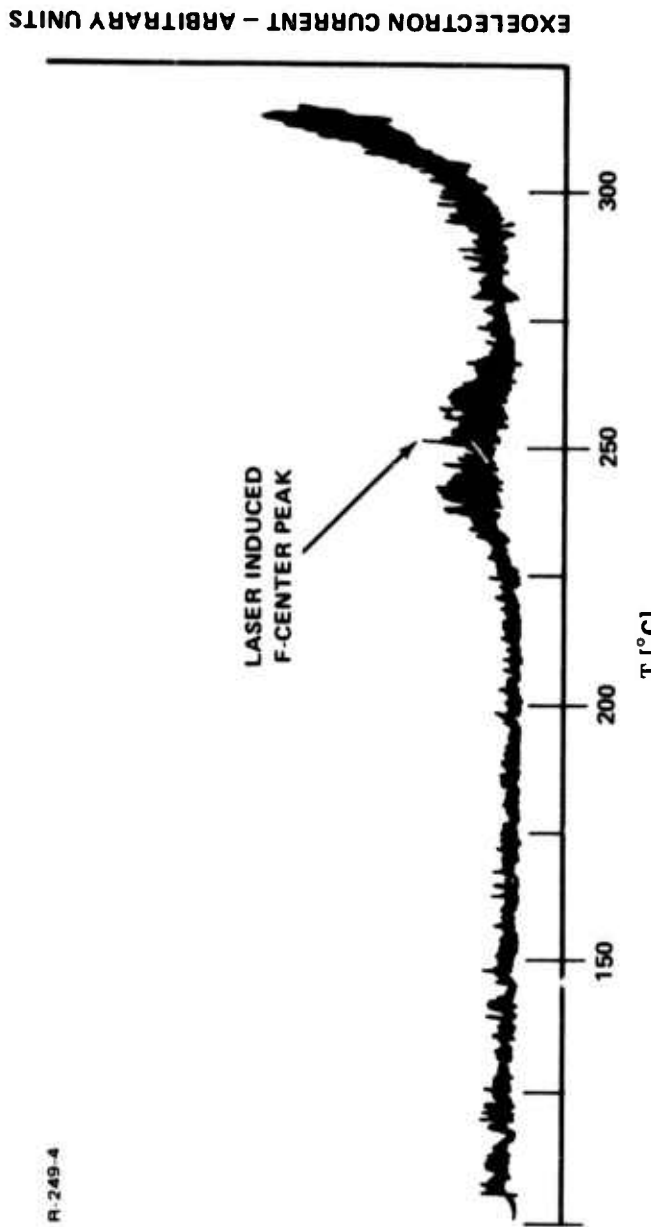


Figure 20 - Laser-induced exoelectron emission from a laser-grade NaCl crystal.

The crystal was previously heated to reduce the type of emission seen in Figure 19. The emission was produced by a single pulse of a ruby laser having a peak flux close to but below the laser damage threshold. (Due to a different heating rate used in different experimental arrangements Figures 18-20 cannot be compared directly.)

SECTION C
CONCLUDING REMARKS

The work described in this report and in the two preceding semi-annual reports (AFCRL-TR-73-0068 and -0591) was performed to investigate the feasibility of laser induced exoelectron emission as a non-destructive test method for laser surface damage. As a result of the theoretical and experimental research carried out in the 18-month contract period, we conclude: Convincing evidence that the exoelectron technique provides easily accessible information on the susceptibility of an optical material to laser surface damage was not obtained. It was shown that the effects, originally believed to lead to characteristic ring-shaped EE images, do indeed exist. Calculations of laser induced exoelectron emission from NaCl show that traps are filled with electrons at laser fluxes close to the intrinsic damage threshold. Experiments have been performed which confirmed the existence of laser induced EE in NaCl. However, in general, the emission current densities are too weak or, in many materials, are completely obstructed by charge emission of different origin for EE to be of any use in NDT of laser surface damage.

The investigations have provided some detailed insight into the damage mechanism, the electron kinetics at intense laser fluxes, and the general exoelectron properties of a variety of materials. This work is by no means complete. Further research, especially experiments, are needed to arrive at a full understanding of laser induced exoelectron emission.

The work will continue under NSF sponsorship.

SECTION 7
ACKNOWLEDGEMENTS

The work reported herein was performed in collaboration with Dr. J. P. Carrico and Mr. A. Schmid who contributed to the construction of the test facilities and performed most of the experiments.

We are indebted to Dr. N. Boling for the use of the Owens Illinois Nd-glass laser. The participation of Dr. P. Kelly (national Research Council, Ottawa, Canada), who performed the numerical calculations, and of Dr. R. K. Rol is gratefully acknowledged.

SECTION 8
REFERENCES

1. Proceedings of the ASTM-NBS Symposia on Laser Damage 1966-1973 (NBS Special Publications 305, 341, 356, 372, 383).
2. P. Bräunlich, *Appl. Phys. Lett.*, 20, 4 (1972).
3. P. Bräunlich, *J. Appl. Phys.*, 42, 495 (1971).
4. P. Bräunlich, B. Rosenblum, J. P. Carrico, L. Hirmel, and P. Rol, *Appl. Phys. Lett.*, 22, 61 (1973).
5. I. W. Krylova, *Z. Chem.*, 13 415 (1973).
6. I. W. Krylova, Proceedings IV Intern. Symposium on Exoelectron Emission and Dosimetry, Liblice, Czechoslovakia (1973).
7. K. Becker, Critical Review in Solid State Sciences (Chemical Rubber Co., Cleveland, Ohio, 1972), Vol. 3.
8. H. Käämbre, Proceedings, IV International Symposium on Exoelectron Emission and Dosimetry, Liblice, Czechoslovakia (1973).
9. M. Bass and H. H. Barrett, *IEEE J. Quant. Elect.*, QE-8, 338 (1971).
10. E. Yablonovitch and N. Bloembergen, *Phys. Rev. Lett.*, 29, 207 (1972).
11. D. W. Fradin, ONR Report NR-372-012, 1973.
12. A. Scharmann, "Thermoluminescence of Geological Materials," D. J. McDougall, ed., Academic Press, London, 1968.
13. A. Bohun, *PTB-Mitt.*, 80, 5 (1970).
14. A. Bohun, *Czech. J. Phys.*, 12, 328 (1962).
15. J. Kramer, *Acta Physica Austriaca*, 10, 327 (1957).
16. V. Bichivin and H. Käämbre, *PTB-Mitt.*, 80, No. 5 (1970).
17. J. Dolejsi, J. Kanturek, A. Bohun and J. Truka, *Czech. J. Phys.*, 8, 548 (1958).
18. B. Sujak and A. Gierszynski, *Acta Phys. Polonica*, 32, 541 (1967).
19. B. Sujak and S. Gasior, *Acta Physica Polonica*, 33 231 (1968).
20. A. Scharmann, *Festkörperprobleme VI* (Vieweg, Braunschweig, 1966), O. Madelung, ed.

21. J. Drenckhan, H. Gross, and H. Glaefeke, *phys. stat. sol.*, (a)2 K51 (1970).
22. B. Rosenblum, P. Bräunlich, and J. P. Carrico, *Appl. Phys. Lett.* (1974) (in press).
23. P. Kelly, *Phys. Rev.* B5, 749 (1972).
24. D. D. Peterson, *phys. stat. sol.*, (a)19, K47 (1973).
25. F. I. Tolpygo, K. B. Tolbygo, and M. K. Sheinkman, *Izv. Akad. Nauk SSSR, Ser. fiz.*, 30 1980 (1966).
26. H. C. Mollenkopf, L. E. Halliburton, and E. E. Kohnke, *phys. stat. sol.*, (a)19, 243 (1973).
27. M. D. Crisp, N. L. Boling and G. Dube, *Appl. Phys. Lett.*, 21, 364 (1972).
28. N. Bloembergen, *Appl. Optics*, 12, to be published (April 1974).
29. Yu. P. Raizer, *Soviet Physics Uspekhi*, 8, 650 (1966).
30. I. M. Catalano, A. Cingolani, and A. N. Minafra, *Phys. Rev.*, 55, 1629 (1972).
31. W. Franz, *Handbuch der Physik*, XVII, 153 (1956), S. Flügge ed, Springer, Berlin.
32. L. V. Keldysh, *Sov. Phys. JETP*, 20, 1307 (1965).
33. J. J. Markham, "F-Centers in Alkali Halides," *Solid State Physics*, Suppl. 8, Academic Press, New York (1966).
34. D. Fradin (private communication), 1973.
35. D. H. Kleinman, *Phys. Rev.*, 125, 87 (1962).
36. G. A. Vorobev, N. I. Lebedeva, and G. S. Nadorova, *Sov. Phys. Sol. State*, 13, 736 (1971).
37. N. Boling (private communication).
38. D. W. Fradin, N. Bloembergen, and J. P. Letellier, *Appl. Phys. Lett.*,
39. M. Bass and H. H. Barrett, *NBS Special Publication*, 372, 58 (1972).
40. D. Fradin and M. Bass, *Appl. Phys. Lett.*, 22, 206 (1973).
41. H. S. Carslaw and J. C. Jaeger, "Conduction of Heat in Solids," sec. ed., Oxford Press, 260 (1959).

42. N. Bloembergen, *Appl. Optics*, 12, (April 1973) in press
43. B. Colson, J. McPherson, and F. T. King, *Rev. Sci. Inst.*, 44, 1964 (1974).
44. P. V. Avizonis, T. T. Doss and R. Heimlich, *Rev. Sci. Instr.*, 38, 331 (1967).
45. L. C. Johnson and T. K. Chu, *Phys. Rev. Lett.* 32, 517 (1974).
46. P. Sladsky, cited in A. Bohun, *Proc. 4th Czech. Conf. Electr. Vac. Phys.*, p. 107, Prague (1968).
47. P. Bräunlich, *Z. F. Physik*, 177, 320 (1964).